Ultraviolet and Optical Line Profile Variations in the Spectrum of Epsilon Persei

D. R. Gies[1], E. Kambe[2], T. S. Josephs, W. G. Bagnuolo, Jr., Y. J. Choi, D. Gudehus,

K. M. Guyton[3], W. I. Hartkopf[4,5], J. L. Hildebrand, A. B. Kaye[6], B. D. Mason[4,5],

R. L. Riddle, J. W. Sowers, N. H. Turner[7], J. W. Wilson, Y. Xiong

Center for High Angular Resolution Astronomy

Department of Physics and Astronomy

Georgia State University, Atlanta, GA 30303

Electronic mail: gies@chara.gsu.edu, kambe@gsasw2.cc.nda.ac.jp, tammy@chara.gsu.edu,

bagnuolo@chara.gsu.edu, phyyjcx@panther.gsu.edu, gudehus@chara.gsu.edu,

uskmg@emory.edu, hartkopf@chara.gsu.edu, jlh@chara.gsu.edu, kaye@lanl.gov,

bdm@draco.usno.navy.mil, riddle@chara.gsu.edu, sowers@chara.gsu.edu,

nils@chara.gsu.edu, wilson@chara.gsu.edu, ying@chara.gsu.edu

Received 1998 October 27; accepted ____________________

Submitted to ApJ

---

[1]Guest Observer *International Ultraviolet Explorer Observatory*

[2]Current address: Department of Geoscience, National Defense Academy
Yokosuka, Kanagawa 239, Japan

[3]Current address: Emory University, Information Technology Division, Atlanta, GA 30322

[4]Visiting Astronomer, Canada-France-Hawaii Telescope, operated by the National Research Council of Canada, the Centre National de la Recherche Scientifique de France, and the University of Hawaii.

[5]Current address: Astrometry Department, US Naval Observatory, 3450 Massachusetts Ave. NW, Washington, DC, 20392

[6]Current address: Los Alamos National Laboratory, Applied Theoretical and Computational Physics (X) Division, Thermonuclear Applications Group, Mail Stop B-220, Los Alamos, NM 87545

[7]Current address: Mount Wilson Observatory, Mount Wilson, CA 91023

ABSTRACT

The rapid variable star, ϵ Per (B0.5 IV-III), displays the largest amplitude profile fluctuations known among the growing number of massive, spectrum-variable stars. Here we present an analysis of a continuous 5 day run of *IUE* UV spectroscopy, and we show for the first time that the systematic, blue-to-red moving patterns observed in high quality optical spectra are also present in the UV photospheric lines. We present cross-correlation functions of the individual spectra with that of a narrow-lined standard that produce a high S/N representation of the blue-to-red moving bump patterns found in individual lines. We then use time series analysis methods to determine the periodic components of the profile variations (after re-registering the spectra to correct for binary motion). There are at least six periods present (ranging from 8.46 hr to 2.27 hr), and most of these signals are also found in optical line variations observed in 1986 (although the relative amplitudes have changed significantly). Furthermore, analysis of a shorter time series of *IUE* spectra from 1984 shows that similar periods were present then. We also present Hα and He I λ6678 profiles obtained with the Georgia State University Multi-Telescope Telescope, which were made simultaneously with *IUE*, and we show that the profile variations are essentially identical in the UV and optical ranges. We rule out rotational modulation and circumstellar gas obscuration as possible causes, and we suggest instead that the variations are the result of photospheric nonradial pulsations of relatively low degree ($l = 3 - 5$). There were significant changes ($\sim 10\%$) in the equivalent widths of the UV stellar wind lines during the *IUE* run, and we suggest that wind strengthening events are related to episodes of large amplitude, constructive interference between the NRP modes. Thus, inter-mode beating may play an important role in promoting wind loss from massive stars.

Subject headings: binaries: spectroscopic — stars: early-type — stars: oscillations (including pulsations) — stars: individual (ϵ Per) — stars: variables: other — ultraviolet: stars

1. Introduction

Rapid spectral and photometric variability is now known to be widespread among massive stars but the root cause or causes of this variability is still a matter of heated debate (Balona 1995; Baade 1998; Harmanec 1999 [H99]). The primary explanations include photospheric nonradial pulsations (NRP), rotational modulation, and circumstellar obscuration. It is important to determine the causal factors because they may play a key role in mass loss processes. This debate has focused in large part on the nature of the large-amplitude variable star, ϵ Per (45 Per, HR 1220, HD 24760, ADS 2888A; B0.5 IV-III, Tarasov et al. 1995 [T95]). This star is a key target because its dramatic spectroscopic and photometric variations are apparently multiply periodic, a characteristic that can only be readily explained in the context of the NRP model.

Bolton (1983) discovered that the spectral variations of ϵ Per take the form of blue-to-red moving bumps in the photospheric absorption lines. Smith (1985, 1986) and Smith, Fullerton, & Percy (1987 [SFP87]) obtained the first high S/N spectroscopic time series of the variations, and their analyses indicated the presence of two periodic signals (with periods of 3.85 and 2.25 hr) in the modulation of the line profiles. Smith and collaborators argued that the variations result from photospheric NRP. Such oscillations effectively divide the visible surface of a star into sectors with differing velocity and temperature fields, and these regions redistribute the flux in a rotationally broadened profile to create a blue-to-red moving bump pattern. Gies & Kullavanijaya (1988 [GK88]) obtained an intensive time series of spectra of ϵ Per in 1986, and they analyzed the spectral variations by calculating power spectra of the spectral intensity at each wavelength point across the profile. They found four prominent signals corresponding to periods of 4.47, 3.84, 3.04, and 2.26 hr. From the variation of the complex phase of the power spectra at a signal frequency with position across the profile, GK88 estimated that the four signals result from NRP modes with orders

$m = -3, -4, -5$ and -6, respectively. This combination of modes creates a complex "beat" pattern in the profile variations. An alternative explanation was suggested by Harmanec (1987, 1989, H99) who noted that these periods are plausibly submultiples of a single period of 1.12 d. Harmanec suggested that the complicated variations might instead be caused by corotating structures situated slightly above the stellar photosphere.

The longer term spectral variations were subsequently investigated by Harmanec (1989), Harmanec & Tarasov (1990), and T95 who demonstrated that ϵ Per is a single-lined spectroscopic binary with a period of 14.076 d. Furthermore, T95 argued that the radial-velocity variations indicate the presence of yet a third star in a wider orbit (with an 11 y period), and they suggested that the wider component might be angularly resolved by speckle interferometry. The system was observed with the Center for High Angular Resolution Astronomy speckle camera and the 3.6-m Canada-France-Hawaii Telescope on 1994.8702 as part of our binary survey of hot stars (Mason et al. 1998). The star was observed in both Strömgren y and b filters, and no companion was found. Thus, if the third star exists, it must either have had an angular separation less than $0\farcs032$ at the time of observation or a magnitude difference greater than $\Delta m \approx 3$.

There is a growing body of evidence that cyclical variability in the stellar winds of OB stars may be related to the rapid photospheric variations observed (Fullerton & Kaper 1995; Cranmer, Massa, & Owocki 1996; Chiueh 1997; Baade 1998; Fullerton 1999). The wind variations often appear as red-to-blue migrating, discrete absorption components (DACs) in the UV P Cygni lines, and these features repeat on time scales related to the stellar rotational period (Massa et al. 1995; Prinja 1998). The wind and photospheric variability periods were found to be similar in two cases, ζ Pup (Reid & Howarth 1996) and HD 64760 (Howarth et al. 1998), and correlated variations in the wind and Hα emission (formed near the photosphere) were discovered by Kaper et al. (1997). This "photospheric connection" probably also plays a role in mass loss from lower luminosity, B-type giants and dwarfs.

Burger et al. (1982) found that a small increase in wind mass loss due to pulsation occurs in the radially pulsating star, BW Vul, and Rivinius et al. (1998a,b) demonstrated that beating between closely spaced periods of photospheric NRP is related to outbursts in the Be star, μ Cen. The subject of this paper, ϵ Per, is an especially interesting target to search for correlated wind and photospheric variability because of the large amplitude of its variations and because the star lies on the borderline in the Hertzsprung-Russell diagram where radiatively driven winds become self-initiating (Cohen, Cassinelli, & MacFarlane 1997).

Here we report on a successful 5 day campaign of near continuous UV spectroscopy of ϵ Per made with the *International Ultraviolet Explorer Satellite (IUE)* during its final year of operation. These spectra record both the blue-to-red moving patterns in the UV photospheric lines and the corresponding changes in the UV wind lines. We recover the photospheric line variations from the noisy *IUE* spectra by calculating the cross-correlation function (ccf) of each spectrum with that of a narrow-lined standard spectrum. We also present near simultaneous, optical spectra made with the Georgia State University (GSU) Multi-Telescope Telescope (MTT) (Bagnuolo et al. 1990). We show that the profile variations observed in the UV and optical ranges are essentially the same. We use time series analysis methods (§3) to derive the periodic content of the variations, and we find that the oscillation pattern has changed in some ways since 1986. The power spectrum results are used to evaluate the NRP modes in the pulsational interpretation (§4), and we compare the photospheric and wind variations in §5.

2. Observations

2.1. International Ultraviolet Explorer

A total of 181 ultraviolet spectra of ϵ Per were obtained with *IUE* in the period 1996 January 10 – 15. Exposures were made approximately every 30 minutes (with actual exposure times varying from 6 to 14 seconds) with a 3 hour gap in the time sampling each day (Table 1). The spectra were made with the large entrance aperture and the Short Wavelength Prime camera in echelle mode (for a resolution $\lambda/\Delta\lambda = 10,000$). The UV spectra were reduced with the standard IUESIPS pipeline routines at the European Space Agency's VILSPA station in Spain (NEWSIPS routines were unavailable at the time).

EDITOR: PLACE TABLE 1 HERE.

The echelle orders were combined and placed on a standard $\log\lambda$ heliocentric wavelength grid that samples the spectrum between 1200 and 1900 Å in 10 km s^{-1} bins. The procedure included re-alignment of the spectra using interstellar lines (after which they were removed by interpolation) and rectification of the spectrum to a pseudo-continuum based on spectral intensity in relatively line-free zones (see details in Penny, Gies, & Bagnuolo 1997). We omitted the Gaussian smoothing procedure we have used in prior work in order to preserve the full resolution of the spectra.

The noisy appearance of the *IUE* spectra (S/N ≈ 15) generally obscures the line profile variations seen in any particular transition, so we adopt the approach of Penny (1996) and Howarth et al. (1998) of studying the variations in the cross-correlation function of the target spectrum with a narrow-lined standard spectrum. The ccf samples the cumulative effects of variations in hundreds of UV transitions, and the final S/N ratio in the ccf is high enough (S/N $\approx 50-100$) to see clearly the moving bump patterns. We selected the narrow-lined star HD 36960 as our standard template. This star has a classification B0.5 V (Walborn 1971) similar to that of ϵ Per B0.5 IV-III (T95) and a low projected rotational velocity of 31 ± 4 km s^{-1} (Gies & Lambert 1992). Thus, the ccf of the spectrum of ϵ Per with that of HD 36960 is predominantly broadened by the lines of ϵ Per alone (effectively convolved with a broadening function of FWHM = 43 km s^{-1} due to the combined effects of the instrumental and standard star rotational broadening). We formed a ccf standard from an average of eight spectra of HD 36960 (SWP29950, 29951, 29959, 29960, 30157, 30158, 30159, 30206) that were processed in the same way as those of ϵ Per. Several features in the UV spectrum of ϵ Per that are exceptionally broad (regions surrounding Lyα, the Si IV λ1400 and C IV λ1550 resonance doublets, and the Al III $\lambda\lambda 1854, 1861$ complex) were set to unity prior to calculating the ccf to avoid broad wings in the result. The final ccfs were rectified to a common background level before analysis (and are shown below in §2.4, Fig. 2).

2.2. Multi-Telescope Telescope

We obtained complementary ground-based spectra of ϵ Per around the time of the *IUE* observations with the GSU MTT, a 1-m equivalent-aperture telescope used for fiber-fed spectroscopy (Bagnuolo et al. 1990). The MTT is an array of nine 0.33-m light-collecting mirrors mounted on an alt-azimuth platform, each mirror feeding starlight through a Barlow lens into a 100 μm diameter optical fiber. In the current configuration, the central mirror is used solely for target acquisition and tracking. The output ends of the fibers are aligned to form an entrance slit to a modified Ebert-type, bench-mounted spectrograph with a CCD camera built by Wright Instruments. The CCD is a Peltier-cooled, EEV chip (CCD-05-11-0-219) with 1152×298 pixels of dimensions 22.5 μm square. These observations were made with a 600 grooves mm^{-1} grating blazed at 1.25 μm. The spectra were made in second order with a blocking filter to remove higher orders (a Corion Corp. LL550 filter which removes light of wavelength shorter than 5500 Å); the CCD is insensitive to first order light. The CCD recorded spectra with a reciprocal dispersion of 0.168 Å pix^{-1} over the range 6500 – 6690 Å, and the spectral resolution is $\lambda/\Delta\lambda = 12,300$ or 0.535 Å FWHM (3.2 pixels as measured in comparison emission lines). Numerous flat field frames were obtained by illuminating the telescope mirrors with incandescent lamps. Wavelength calibration was accomplished by imaging the spectrum of a Th-Ar hollow cathode tube via two optical fibers that place the comparison spectrum above and below the stellar spectra on each exposure. An additional wavelength calibration frame was made by illuminating each telescope mirror with the Th-Ar source (in addition to the two standard comparison fibers) to determine the spatial offsets of each science fiber relative to the comparison fibers. We obtained 54 spectra in total distributed over 6 nights of observation (Table 2). The exposure time for each spectrum was 20 minutes, and the final S/N ratio ranges from 60 to 400 (depending on the number of aligned mirrors in use and the weather conditions at the time).

EDITOR: PLACE TABLE 2 HERE.

The spectra were reduced using standard methods with IRAF[8] packages. In brief, each frame was subject to dark, bias, and scattered light subtraction, and then one-dimensional spectra were extracted for each illuminated fiber. The flat field division was done after this extraction (to avoid numerical problems where the flat frames are poorly exposed). The spectra for each exposure were wavelength calibrated, combined on a common wavelength

[8]IRAF is distributed by the National Optical Astronomy Observatories, which is operated by the Association of Universities for Research in Astronomy, Inc., under contract to the National Science Foundation.

grid, and rectified to unit continuum. Then all the spectra were transformed to a uniform heliocentric wavelength grid. As a final step, we removed the atmospheric telluric lines near Hα using observations of a rapidly rotating A-star (see Gies & Wiggs 1991).

2.3. Orbital Velocity Corrections

T95 determined that ϵ Per is a single-lined spectroscopic binary with a 14.076 day orbit. We need to remove the orbital motion of the star and align the spectra in its reference frame before analyzing the line profile variations (we neglect small light travel time corrections which amount to no more than 17 s). Here we describe measurements of the orbital motion and how we shifted the spectra to compensate for the orbit.

The rapid profile variations introduce a significant distortion in any kind of radial velocity measurement, and since these variations peak in amplitude at line center (see Fig. 9 below), the line wings offer the least affected portions for our purposes. We used the double-Gaussian bisector method of Schneider & Young (1980) to measure the wing radial velocities. Each line profile or ccf was cross-correlated with a template consisting of two oppositely signed Gaussians separated by an amount $2\Delta\lambda$, and the zero crossing position of the resulting cross-correlation function was used to determine the effective radial velocity. We used $\Delta\lambda = 180$ km s^{-1} and Gaussians with HWHM = 40 km s^{-1} to measure radial velocities of the UV ccfs and the Hα and He I $\lambda 6678$ absorption lines (however the results are insensitive to the exact values of these parameters). We estimated the errors in the relative radial velocities from the UV ccfs by measuring the scatter in data from a time interval when the profile variations were minimal (in the heliocentric Julian Date range, HJD $2,450,095.8 \pm 0.1$) which yields $\sigma_{UV} = 1.8$ km s^{-1}. We found good agreement between velocities from Hα and He I $\lambda 6678$, and the scatter between these measurements indicates individual radial velocity errors of approximately $\sigma_{MTT} = 2.1$ km s^{-1}. Unfortunately, we have no radial velocity standard star measurements from the MTT at the time of the campaign, but prior work on a similar star with the same instrumental set up (Gies et al. 1996) demonstrated that systematic errors are less than 2 km s^{-1} (compared to results from the University of Texas McDonald Observatory 2.1-m coudé spectrograph). Thus, we used the optical results to place the UV measurements on an absolute scale by taking the difference in the mean of the average optical velocities and the mean of the ccf relative velocities (+11.3 km s^{-1}) to transform the ccf velocities to an absolute scale. The final radial velocities are listed in Table 1 (UV ccfs) and Table 2 (MTT) and are plotted in Figure 1.

EDITOR: PLACE FIGURE 1 HERE.

The radial velocity data show a systematic increase in the main part of the observing run followed by a decrease in data from one week later. There are rapid fluctuations caused by the profile variations (hourly time scale and $\sim$ 10 km s^{-1} in amplitude) superimposed upon the long term trends. The dotted line in Figure 1 shows the orbital velocity curve predicted according to the triple star solution advocated by T95 (their "solution 5" with P = 14.075897 d, T = 2,447,767.411, K_1 = 16.0 km s^{-1}, e = 0.528, ω = 107°.7, and systemic velocity at the time of our observations, γ = 5.80 km s^{-1}). While the general shape of the curve appears to match the observations, it is offset in time and/or radial velocity by a constant amount. We decided to fit our data by translating the expected curve in time only because the alternative of making a velocity correction would require a velocity shift ($\sim$ 6 km s^{-1}) much larger than any expected systematic error and the resulting fit would be poor for the penultimate night of MTT observations. Thus, we set the systemic velocity to the predicted value from T95 and adjusted the time of periastron only. We find T = HJD 2,450,101.77 $\pm$ 0.15 for this fit (with residuals of 4.4 km s^{-1} r.m.s. which are not unexpected for the suspected pulsational effects), and this working fit is shown as the solid line in Figure 1. We applied the fitted radial velocities for each observation to shift each of the ccfs and optical profiles to the rest frame of the star (thus removing the binary motion). There is no evidence of the secondary (or tertiary) in our optical spectra or ccfs, and we will assume that the profile variations can be assigned entirely to the spectrum of the primary star.

2.4. Comparison of UV and Optical Line Profile Variations

The UV ccfs corrected for orbital motion appear in Figure 2 in a gray-scale diagram in which differences from the mean ccf are depicted as bright (dark) for deviations above (below) the mean. The blue-to-red moving bump pattern is clearly seen throughout the sequence but with varying strength and degree of complexity. The same kinds of variations are observed in the individual line profiles in the optical spectra. Figure 3 shows a gray-scale diagram of the variations found in the MTT spectra. The bump patterns are clearly evident in Hα and He I $\lambda 6678$ (and also in the weak C II $\lambda 6578, 6582$ doublet). The patterns appear more diffuse in Hα which is probably due to Stark broadening of the intrinsic photospheric profile.

EDITOR: PLACE FIGURE 2 HERE.

EDITOR: PLACE FIGURE 3 HERE.

Our original goal of obtaining truly simultaneous UV and optical spectroscopy was only realized for about 3 hours around HJD 2,450,096.75 (the lower half of Fig. 3). Nevertheless, we show here that the observed variations appear to be identical in the two spectral ranges at least over this short interval. We compare the differences from the mean profile of the

UV ccfs and He I λ6678 line as a function of time in Figure 4. We first normalized the difference profiles relative to the core depth in each case, and we then smoothed the MTT spectra of He I λ6678 with a Gaussian transfer function of FWHM = 40 km s^{-1} in order to make the spectral resolution comparable to that of the UV ccfs. The time evolution of these difference profiles is the same within errors, and so we are confidant that the variations so well documented in the UV ccfs are the same ones that are observed in high S/N spectroscopy of optical lines.

EDITOR: PLACE FIGURE 4 HERE.

We applied the same renormalization and smoothing to the He I λ6678 difference profile sequences from HJD 2,450,093.6 and 2,450,096.6, and these are inserted in the gaps in the *IUE* data in Figure 2 to demonstrate again the similarity of the patterns (below, however, we analyze the profile variations in the two regimes independently). The MTT observations in these two gaps show a seamless progression between the bounding *IUE* observations, and we conclude that both the UV and optical photospheric lines exhibit the same kind of profile variability.

3. Period Analysis

3.1. Methods

The moving bump patterns observed in the UV ccfs are clearly repetitive but are also irregular in bump spacing and amplitude. Our goal here is to determine the periodic content of the variations, and in particular if the same periods exist that were detected in earlier studies. Any investigation of time variability is limited by the duration of and gaps in the observation sequence, and the consequences of these limitations are well illustrated in the window function (cf. Roberts, Lehár, & Dreher 1987). The window function for the *IUE* spectral sequence is shown in the upper panel of Figure 5. Because the *IUE* observations are essentially continuous over a 5 d interval (with only small diurnal gaps), the signal power is concentrated in a central peak (of FWHM equal to the inverse of the full duration of observations) with relatively small outlying peaks. On the other hand, the window function for the MTT optical observations (lower panel of Fig. 5) has a narrower central peak (because of the longer elapsed time between first and last observations) and a huge array of accompanying alias peaks (dominated by ± 1 cycle d^{-1} aliases) introduced by the large gaps in the optical data sampling. The observed periodogram of any time variable quantity is a convolution of the window function with the actual periodic signals, so the periodic signals will be much easier to find in periodograms of the *IUE* data.

EDITOR: PLACE FIGURE 5 HERE.

We determined periodicities using three methods of analyzing the line-intensity variations across the profiles. First, we used the Fourier transform methods of Roberts et al. (1987) to construct the "dirty" periodograms (DPs) for time series at each wavelength point across the profile (see GK88), and we then summed the power in the wavelength dimension and measured peak positions in the summed periodogram. We decided not to apply the CLEAN algorithm to deconvolve the periodic signals from these DPs (Roberts et al. 1987) because the alias problems are minor for the *IUE* data and CLEAN does not significantly improve the results. Furthermore, CLEAN results are ambiguous for the optical time series for which the alias problems are severe.

The second procedure is the so-called prewhitening (PW) method. We applied least-squares fitting of a sinusoid to the temporal variations of the line profile at each wavelength point (with a single period but variable amplitude and phase with wavelength position), and we then subtracted sinusoids sequentially from the observed time series. This method is almost equivalent to using the CLEAN method with a gain of unity, in which we sequentially subtract the maximum peak and its alias patterns from periodograms in frequency space.

The third method is the simultaneous, least-squares fitting of multiple sinusoids to time series at each wavelength point (MSF method; Kambe et al. 1997). Because of limits on computational time, we searched no more than three new frequencies simultaneously. Other frequencies are fixed in the parameter search but all the amplitudes and phases of N sinusoids are re-determined in each search.

The significance of the sinusoidal fits is gauged by the Akaike information criterion (AIC; Kambe, Ando, & Hirata 1990) which is defined by

$$\begin{aligned} AIC(N) = & \quad -2 \times (\text{maximum log likelihood of the model}) \\ & \quad +2 \times (\text{number of free parameters in the model}) \\ \sim & \quad \textstyle\sum_{i,j}^{N_t,N_\lambda} \frac{\sigma^2_{s(i,j)}(\hat{\underline{\omega}},N)}{\sigma_i^2} + 2N(1+2N_\lambda) \end{aligned} \tag{1}$$

where

$$\sigma^2_{s(i,j)}(\hat{\underline{\omega}}, N) = \quad (y_{i,j} - \textstyle\sum_k^N a_{k,j}\sin(\omega_k t_i + \alpha_{k,j}))^2. \tag{2}$$

Here, $y_{i,j}$ is the deviation of the line depth from the average depth at each wavelength point λ_j at time t_i, and σ_i^2 is the variance in the continuum. The hat mark in $\sigma^2_{s(i,j)}(\hat{\underline{\omega}}, N)$ describes the best set of frequencies for each of the N sinusoidal signals.

By introducing the AIC, we have one criterion which combines information on the goodness-of-fit from time sequences for all wavelength points. The first term of equation (1) corresponds to the residuals in units of the variance (i.e., the square of noise) of the continuum of each spectrum. In general, the statistical significance of adding a new sinusoid can be determined by the size of the decrease between AIC(N) and AIC($N+1$). In practice, however, statistical criteria are only applicable when the data are well reproduced by a relatively small number of sinusoids with Gaussian noise. In our case, we found that adoption of statistical criteria led to the inclusion of artificial peaks due to systematic errors in the data and/or harmonic peaks of stronger signals due to the slightly non-sinusoidal nature of the variations. Thus, we chose to terminate the search if the derived periodic signals appeared to be spurious (for example, were not seen over a wide portion of the profile).

3.2. UV Cross Correlation Functions

We first made periodograms to search for signals in the UV ccf radial velocities and equivalent widths, but we found no significant periodicities. This exercise reassures us that we have adequately removed the radial velocity shifts associated with orbital motion (§2.3). We then used our time series methods to investigate periodicities in the UV ccfs at each radial velocity (cross-correlation offset) position. The DPs are illustrated in a gray-scale diagram in Figure 6 as a function of profile position and frequency. True periodicities appear as horizontal bars that span the line core, and visual inspection suggests the presence of at least 4 periodic signals.

EDITOR: PLACE FIGURE 6 HERE.

The results of the MSF procedure are listed in Table 3. The first column is the number of sinusoids fit, N, the second column shows how the AIC decreases with each additional sinusoid (for $N_\lambda = 41$, $N_t = 181$), and the third column gives the new sinusoidal period detected (so that the table lists the signals from strongest to weakest amplitude). We only solved for a maximum of 3 sinusoids at any given stage in the search, and since the stronger signals were consistently recovered at each stage, we fixed their periods once we had added

3 more periodicities in the fit (for example, the value of the first periodicity was fixed at $N = 4$, etc.). The fitted peaks were found by a numerical grid search in frequency space with a resolution at least three times (thirty times for $N < 4$) finer than the reciprocal of the total length of the observations. After such searches, however, parameters for all the peaks were re-determined as accurately as their theoretical error estimates (Kovacs 1981). Column 3 lists these final period determinations with the errors in the last quoted digit given in parentheses (based on theoretical estimates which may be low). The period for $N = 6$ is one day, and this originates in diurnal variations of certain bad pixels in the *IUE* spectra.

EDITOR: PLACE TABLE 3 HERE.

Column 4 of Table 3 gives the resulting periodicities from the sequential fitting of single sinusoids (PW method), and these results are in excellent agreement with those from the MSF procedure. Finally, column 5 lists the periodicities measured directly from the cross-profile summed DPs, and errors are derived strictly from the HWHM of the peaks. All of the 7 periodicities found by the MSF and PW methods were easily measured in the summed DP. The AIC value can be reduced further by adding more sinusoidal components. After subtraction of six peaks, for example, the residuals are still 1.9 times larger than the continuum noise on average (see the first term of eq. [1]). However, we tentatively limit the candidate periods to those listed in Table 3 since the heights of the remaining peaks are lower than that of the suspected artificial peaks.

3.3. Optical Lines

The aliasing problems with the optical time series are severe (Fig. 5), and all of the methods of period determination become problematical after identification of the first few periodicities. Nevertheless, it is useful to investigate the optical results because the long duration of the optical sequence can potentially yield smaller errors for the period estimates. Rather than treating the optical data completely independently, we instead assumed that the main signals found in the UV time series are probably also present in the optical series and we focused our attention on local peaks in the summed DPs for Hα and He I λ6678 that correspond to those in the IUE power spectrum.

There are two lines of evidence that support this approach. First, we showed above (§2.4, Fig. 4) that the UV and optical profile variations appear identical in intervals of overlap. Secondly, we can estimate what the optical periodogram should look like by convolving the the signals extracted from the UV time series with the window function for the optical spectra. The third panel of Figure 7 shows the summed DP for the UV ccfs while the top panel shows the corresponding periodogram from the MTT optical spectra (He I λ6678). The second panel from the top shows the expected optical results formed by convolving the UV signals listed in Table 3 with the optical window function (after omitting the spurious $N = 6$ signal and slightly adjusting the frequencies of the four main signals according to the He I λ6678 analysis). The agreement is good, and this indicates that the optical and UV variations are consistent with a common set of periodic signals.

EDITOR: PLACE FIGURE 7 HERE.

The final two columns in Table 3 list the periods derived from measuring the local peak positions that correspond to the UV signal periods in the summed periodograms of the optical lines. The peaks corresponding to the weak signals are not easily identified in the optical periodograms because of the aliasing problems, and no entries are listed for these.

3.4. Comparison to Previous Results

The discovery of multiple periods in the relatively continuous observations from *IUE* provides a secure basis to reevaluate the periods determined from earlier observations that had significant diurnal gaps and related aliases. We list in Table 4 a comparison of the *IUE* based periods with earlier reported results from extended time series of optical spectroscopy made since 1984.

EDITOR: PLACE TABLE 4 HERE.

We begin with a comparison of our results with the study by GK88 made with 2.7-m telescope at the University of Texas McDonald Observatory. The summed DP of the GK88 observations of variations in Si III λ4552 is illustrated in the fifth panel down of Figure 7 for direct comparison with the *IUE* results (third panel of Fig. 7). The McDonald Observatory sequence is based upon a 5 d run which included one cloudy night, and the window function for these observations displays large amplitude aliases (see GK88, Fig. 9). We can test the hypothesis that the periodic signals were the same in 1986 and 1996 by convolving the signals from the *IUE* periodogram with the window function for the 1986 GK88 observations. The resulting convolution is shown in the fourth panel of Figure 7, and the agreement is generally reasonable between the convolved 1996 and observed 1986 power spectra. There are, however, two marked differences that indicate that the relative amplitudes and perhaps frequencies of the spectral variations have changed over 10 years. The first difference is the dramatic increase in the strength of the signal near 5.91 cycle d^{-1} which has emerged from near obscurity in the 1986 data to become the most prominent signal in 1996. The second difference is the increase in strength of the 5.28 cycle d^{-1} between 1986 and 1996. The period appears to be somewhat longer in the 1996 results (Table 4), but we caution that this signal is separated by approximately 1 cycle d^{-1} from the very strong 6.25 cycle d^{-1} signal, and period estimates from the 1986 time series may suffer from alias problems.

Table 4 gives the 4 periods found by GK88 plus two sets of periods derived independently for the same time series of Si III variations (Fullerton & Aerts 1993 [FA93]; Telting & Schrijvers 1997 [TS97]). In addition, we reanalyzed the variations using the MSF method described above. All of these studies agree on the presence of periodicities at 5.28, 6.25, and 10.58 cycle d^{-1} (the latter two were first measured by SFP87 in 1984 observations), and the strong 6.25 cycle d^{-1} period also appears in He I $\lambda6678$ measurements made at the Crimean Astrophysical Observatory between 1988 and 1992 (T95; H99). The main difference in the studies of the 1986 variations is the detection of the 6.84 cycle d^{-1} signal by all but GK88. Their CLEAN deconvolution of the periodogram apparently assigned the power in this signal to the +1 cycle d^{-1} alias at 7.90 cycle d^{-1}. Based upon the *IUE* results, it now appears that the 6.84 cycle d^{-1} frequency is the correct choice. Note that the frequency separation between this signal and the now dominant 5.91 cycle d^{-1} signal is again uncomfortably close to 1 cycle d^{-1}, and it is possible that the period searches have assigned some of the power from the latter to the former (although the 5.91 cycle d^{-1} signal was found as a weak periodicity by the MSF method). The other signal found in the *IUE* power spectrum (at 2.83 cycle d^{-1}) is too weak in the 1986 data for confirmation.

The star was also observed by *IUE* for 0.6 d in 1984 during the ground-based investigation by SFP87. We retrieved these 13 high dispersion spectra from the *IUE* archive, and created UV ccfs in the same way as we did for the recent spectra (§2.1). This short sequence of ccfs is illustrated in Figure 8 (in the same format as Fig. 2). Ground based spectra were obtained simultaneously by SFP87 during the second half of the sequence, and once again there is good agreement between the variations observed in the UV and visible (compare with Figs. 8 and 9 in SFP87). The summed power spectrum of the UV ccf variations is shown in the bottom panel of Figure 7. The short duration of the observations results in very poor resolution in frequency space, and we can only conclude that the variations seen in 1984 are approximately consistent with those observed in succeeding years.

EDITOR: PLACE FIGURE 8 HERE.

TS97 and H99 point out the nearly 2 : 1 ratio of the (5.28, 10.59) and (6.25, 12.53) cycle d^{-1} pairs. It is possible that these two higher frequencies are simply the first harmonics of the lower frequencies that result from the non-sinusoidal shape of the variation. We will return to this possibility in the next section.

4. NRP Modal Analysis

The second, wavelength dimension of the time series analysis shows how the periodic signals change with position across the profile. The complex phase of the periodogram at a signal frequency is the cosinusoidal phase of the variation at the mean time of the observations (HJD 2,450,095.4149 for the *IUE* sequence), and so the variation in complex phase across the profile yields the number of cycles ("bumps") visible at any instant. The spectral lines of early-type stars like ϵ Per are dominated by rotational broadening so that profile positions from blue-to-red correspond to flux contributions from the approaching to the receding stellar limb. If the rapid variations are caused by NRP, then the difference in complex phase between line wings, $\Delta\Psi$, is directly related to the number of oscillations across the visible hemisphere. GK88 interpreted the variations in ϵ Per within the context of the NRP model, and they made the simplifying assumption that the oscillations were sectoral modes (those with nodes only at the poles and with NRP harmonic degree, l, equal to the absolute value of the azimuthal order, m). For this special case, $|m| \approx \Delta\Psi/\pi$, where $\Delta\Psi$ is measured in radians. TS97 explored the complex phase difference across profiles for an extensive series of model NRP profile variations, and they found that $\Delta\Psi$ is generally related to l rather than m (although the latter may be estimated from the phase difference across the profile at the first harmonic frequency). Here we apply their prescription to determine the NRP degree, l, of the signals found in the *IUE* time series.

The variations in phase and amplitude across the UV ccf profile for each of the 6 main signals are illustrated in Figure 9 (taken directly from the DPs; these results differ negligibly from the parameter fits of the MSF method described above). We define phase here as the cosinusoidal phase of the inverted ccf (Fig. 6) so that the convention is identical to that for absorption lines. The power generally extends to or beyond the rotational broadening limits ($V \sin i = 134$ km s^{-1}; SFP87), and likewise a consistent trend in phase often extends beyond these boundaries. This is probably the result of broadening introduced in the cross-correlation process and correlation with neighboring lines in the dense UV spectrum. We measured $\Delta\Psi$ consistently between the $V \sin i$ limits, although we caution that this approach may underestimate the full variation (see Fig. 2 in TS97). We then estimated l according to the empirical result of TS97, $l \sim 0.1 + 1.09|\Delta\Psi|/\pi$, and these values are listed in column 3 of Table 5. We also measured l from the phase differences of the strong signals in the periodograms of the He I λ6678 and Hα variations, and these are listed in columns 6 and 7, respectively. We include in column 8 the resulting l values from our re-examination of the Si III λ4552 (1986) variations, followed by earlier estimates based upon the same data set by GK88 and TS97 (in columns 9 and 10, respectively).

EDITOR: PLACE FIGURE 9 HERE.

EDITOR: PLACE TABLE 5 HERE.

Kennelly et al. (1998) describe an alternative method to determine l from time series data based on a second Fourier transform in the wavelength dimension (termed Fourier

Doppler Imaging). The complex periodograms are first transformed from velocity, V_r, to a grid based on $\phi = \sin^{-1}(V_r/V \sin i)$, a parameter used to measure distance perpendicular to the projected rotational axis of the star. The periodograms are then Fourier transformed in the ϕ dimension at each frequency point. The naive expectation that the position of peaks in this transformed dimension corresponds to the number of cycles of oscillation around the stellar equator, $|m|$, is not fully borne out in numerical experiments by Kennelly et al. who find that this diagnostic is a better measure of l (confirming the results of TS97). Kennelly et al. refer to the transformed dimension as the "apparent NRP degree" which is generally equal to or slightly larger than the actual NRP degree, l. The 2-dimensional power spectrum for the UV ccfs is illustrated in Figure 10. The dominant signals seen previously in radial velocity space (Fig. 6) now appear centered over the apparent NRP degree corresponding to the spatial frequency of the bumps. Our measurements of the positions of the 6 main peaks are given in column 4 of Table 5.

EDITOR: PLACE FIGURE 10 HERE.

We expect that the l values derived from measuring $\Delta\Psi$ between the $V \sin i$ boundaries are underestimates (TS97) while the results from the method of Kennelly et al. (1998) are overestimates, and these trends are found in the results listed in Table 5. We also list in column 5 of Table 5 an upper limit on l for sectoral modes based on the slope, $d\Psi/dV_r$, at profile center (see GK88, eq. 11). There is reasonable agreement overall between the l estimates from all these methods and between the results from 1986 and 1996, and we give our adopted values in the final column of Table 5.

The numerical simulations made by TS97 show that the first harmonic of a signal frequency may often appear in the periodograms, and they find that the NRP order, m, can be found from the complex phase difference at the harmonic frequency:

$|m| \sim -1.33 + 0.54|\Delta\Psi_1|/\pi$. They note that the 2.27 hr signal could be the first harmonic of the 4.54 hr signal in the profile variations of ϵ Per, and they suggest that the two signals correspond to one tesseral mode with $l = 3$ and $|m| = 2$. Our measured phase differences give similar results ($l = 3$ and $|m| = 1$) if the 2.27 hr signal is a harmonic, but we need to treat this conclusion with caution. TS97 find that the model power distribution across the profile is similar in the main and harmonic signals, but the observed distributions have different widths (Fig. 9). Furthermore, TS97 show that there is a general relationship between the complex phases of the fundamental and harmonic frequencies at line center, $2\Psi_0 - \Psi_1 = 1.50\pi \pm 0.06\pi$ (where the phase convention is based on sinusoids). After transformation to the sine convention (by adding 0.5π to the phases), we measure the phase differences to be $2\Psi_0 - \Psi_1 = 1.1\pi, 1.4\pi$, and 1.0π ($\pm 0.2\pi$) in the central periodograms of the UV ccfs, He I λ6678, and Si III λ4552, respectively. It is not clear whether or not the differences between the observed and predicted values are significant.

5. Wind Line Variations

We return here to the question posed in the introduction about possible connections between the rapid variability and mass loss via stellar wind. We examined the *IUE* spectra in the vicinity of the Si IV λ1400 and C IV λ1550 doublets to search for any obvious patterns of variability. These lines appear as strong and broad absorption features in ϵ Per rather than full fledged P Cygni lines (see Walborn, Parker, & Nichols 1995), but their exceptional width implicates their formation at least partially in the wind. We found no clear evidence of moving features (like the DACs) nor of rapid variability of any kind. However, both features appeared to show episodes of slow growth and decline during the observing run. We measured equivalent widths of these features over the ranges 1391 – 1406 Å and 1545 – 1552 Å and calculated normalized deviations for each feature ($(W_\lambda - < W_\lambda >)/ < W_\lambda >$

where $< W_\lambda >= 6.5$ and 3.5 Å for Si IV λ1400 and C IV λ1550, respectively. The equivalent width variations (Fig. 11) are synchronized in time and appear to be relatively stronger in C IV λ1550.

EDITOR: PLACE FIGURE 11 HERE.

The two episodes of strengthening are separated by approximately 2.3 d, much longer than the periods associated with the rapid profile variations. Nevertheless, this timescale may be comparable to intervals of strong beating between the periodicities. We show in Figure 11 the central depth of the UV ccfs plus the predicted time evolution based on the sum of the 6 signals derived by time-series analysis. There is a suggestion in this figure that the strengthening of the wind features appears to follow times of strong constructive interference between periodicities. It is possible that the apparent match is coincidental since there are only two episodes during the run (and since relatively large variations at the beginning of the sequence are not accompanied by wind line changes). However, the results in Figure 11 do indicate that wind variations occur on timescales related to those associated with beating of the rapid periodicities.

6. Discussion

Many OB stars display profile variability like that seen in ϵ Per (although usually at much lower amplitude), and if we can reliably identify the cause of the variations in this star, then we may be close to explaining the phenomenon in general. There are three categories of models that could potentially explain the rapid variations in the spectra of ϵ Per: rotational modulation, circumstellar structures, or NRP. We argue here that only the pulsation model is consistent with the observations presented above.

We first confirm that the bump patterns migrate too quickly across the profiles to be explained by stellar rotation (GK88; Harmanec & Tarasov 1990; H99). If the moving bumps are caused by stellar rotation, then the implied rotation period is approximately $l\ P$, the time for an entire set of cycles to cross the star's central meridian (the so-called "superperiod"). All the periodic signals would presumably have the same superperiod, and thus the stellar angular rotation rate would be given by the slope of the signals in the apparent degree, l, versus frequency, $\nu = 1/P$, diagram (Fig. 10), $\Omega_{\rm app} = < 1/(l\ P) > \approx \triangle\nu/\triangle l$ (Kennelly et al. 1998). Our results yield $\Omega_{\rm app} = 1.8 \pm 0.4$ d^{-1}. On the other hand, the rotation rate cannot exceed the critical break-up velocity which depends upon the stellar mass and radius. T95 estimate that the mass is approximately $13.5 \pm 2\ M_{\odot}$. The radius of the star can be calculated from the recent *Hipparcos* (ESA 1997) parallax data ($\Pi = 6.06$ mas $\pm$ 0.82 mas) and an estimate of the stellar angular diameter based on the ratio of observed to emitted flux. We took the observed flux between 1200 and 10000 Å from a combination of *IUE* FUV and NUV spectra and optical spectrophotometric scans from Alekseeva et al. (1996), and we compared to this to fluxes from a line blanketed, LTE model by Kurucz (1994) for $T_{\rm eff} = 27,600$ K, $\log g = 3.85$, solar abundances, and a microturbulent velocity of 8 km s^{-1} (parameters from T95). The best fit parameters are a reddening of $E(B-V) = 0.10 \pm 0.02$ (for an assumed ratio of total to selective extinction, $R_V = 3.1$) and angular diameter of 0.37 ± 0.02 mas, and with the *Hipparcos* distance, this implies a linear radius of $R_{\star}/R_{\odot} = 6.6 \pm 1.0$ (in agreement with estimates of $R_{\star}/R_{\odot} = 6.9 \pm 0.2$ and 6.0 ± 0.9 from T95 and H99, respectively). The star may actually be slightly smaller than this since we have not accounted for any (small) flux contribution from the companion stars. Then the critical angular rotation rate is (GK88, eq. [5]) $\Omega_{\rm crit} = 1.02 \pm 0.23$ d^{-1} which is significantly lower than $\Omega_{\rm app}$. Thus, unless our mass and radius estimates are incorrect, the bump passage rate implies a rotation rate well in excess of the critical value, so we can rule out models involving "spots" fixed to a rotating star.

Harmanec & Tarasov (1990) and H99 advocate models in which the profile variations are caused by corotating structures slightly above the stellar photosphere. Circumstellar gas usually creates Balmer emission but we see no evidence of Hα emission in our spectra, nor has any been reported by previous investigators. We noted above (see Fig. 3) that the bump patterns are much more diffuse and broad in Hα than in He I λ6678 (which accounts for the much reduced amplitude of the higher order, 2.27 hr signal in the Hα periodogram). The simplest explanation is that the bump patterns suffer the same collisional Stark broadening as do the photospheric lines which implies that the patterns form in regions of photospheric density. In fact, we expect that features formed in a circumstellar disk would normally appear as very narrow features confined to the line core (as observed in Be shell stars). Furthermore, our results show that the patterns are both multiply periodic and stable in period over time scales of a decade, and it is difficult to imagine how circumstellar gas structures that are subject to differential rotation could survive over such a duration. Thus, we very much doubt that the rapid variations are caused by circumstellar structures. Harmanec & Tarasov (1990) and H99 suggest that all the observed periods are actually submultiples of a single period of 1.12 d. There is no evidence of this period in our results (Fig. 6), and the new periodicities we have detected in the 1996 data (including the strongest, 4.06 hr signal) are not integer submultiples of their proposed period. Note that the frequency differences between the 4.54/3.84 hr and 4.06/3.51 hr pairs of signals correspond to a beat period of approximately 1.05 d, and possibly it is the patterns that result from interference between these periodicities that led Harmanec to focus on this timescale.

This leaves multi-mode NRP as the best working explanation for the observed periodic variations (SFP87; GK88; TS97). We found that the variations appear very similar in the UV and optical ranges, and this suggests that the pulsations are predominantly manifested as velocity fields rather than temperature fields (since otherwise the differences in limb darkening and the flux derivative with temperature between the UV and optical would create differences in the appearance of the profile variations). The time-series analysis of the UV ccfs indicates the presence of at least 5 pulsational modes of relatively low degree ($l = 3 - 5$), and most of these signals were probably present in 1986, albeit with different amplitudes. This opens up the prospect of astroseismological studies of an important target among the massive stars, and we plan to pursue such investigations in future papers. We note here, however, that there appears to be a common frequency spacing between the 4.54/4.06 hr and 3.84/3.51 hr pairs of 0.6 d^{-1} which could plausibly be due to rotational splitting of the modes. We note for completeness that an extension of the MSF analysis of the UV ccfs to $N = 12$ sinusoids yields weak signals at 4.251 hr and 4.716 hr which again have a separation of 0.6 d^{-1}. If we speculatively assume that this frequency difference represents the angular rotation rate, then the equatorial velocity would be approximately 200 km s^{-1} for a radius of $6.6 R_\odot$, and this is consistent (for an inclination, $i = 42°$) with the observed projected rotational velocity, $V \sin i = 134$ km s^{-1}. We doubt that the angular rotation rate can be much greater than 0.6 d^{-1} because higher values imply a low rotational axis inclination which would allow us to see over the pole and view red-to-blue moving features from the far longitudes, and such reverse motion has never been seen in this star's spectral lines.

Finally we return to the possibility of a "photospheric connection" between pulsation and mass loss. We observed two episodes of wind-line strengthening separated by about 2.3 d during the 5 d *IUE* run (Fig. 11). The recurrence times for wind variations are often found to be close to the stellar rotation period (or some integer sub-multiple thereof; Fullerton & Kaper 1995; Prinja 1998). In the case of ϵ Per, the longest possible rotational period (for an inclination, $i = 90°$) is 2.5 d, so the observed time interval between wind events may be comparable to the rotational period. We noted in §5 that both events appear to be preceded by episodes of large amplitude bump passages caused by constructive interference of the NRP modes. Thus, we tentatively suggest that beating between modes may play a key role in promoting wind mass loss from this star. Rivinius et al. (1998a,b) also found that beating between closely spaced pulsational periods was related to mass loss episodes in the Be star, μ Cen. Thus, if multiple mode pulsations are common among massive stars, we should expect that interference between modes will play an important role in promoting episodic mass loss in general. Finally, we note that if rotational mode splitting occurs among early-type pulsators, then the beating time scales may be similar to the rotational periods, which may explain why the wind variation time scales are similar to the rotational periods.

We thank the *IUE* Observatory staffs at NASA/GSFC and ESA/VILPSA (especially Dr. Enrique Solano) for their help in making these observations. We also thank Dr. Myron Smith for his suggestion to analyze the 1984 *IUE* spectra of ϵ Per obtained by Dr. Mark Giampapa and him. Support for this work was provided by NASA grant NAG5-2979. Institutional support has been provided from the GSU College of Arts and Sciences and from the Research Program Enhancement fund of the Board of Regents of the University System of Georgia, administered through the GSU Office of the Vice President for Research and Sponsored Programs. The work of A. B. Kaye was performed under the auspices of the U. S. Department of Energy by the Los Alamos National Laboratory under contract No. W-7405-ENG-36. We gratefully acknowledge all this support.

REFERENCES

Alekseeva, G. A., et al. 1996, Baltic Astron., 5, 603

Baade, D. 1998, in Cyclical Variability in Stellar Winds, Proceedings of the ESO Workshop Held at Garching, Germany, 14 - 17 October 1997, ed. L. Kaper & A. W. Fullerton (Berlin: Springer), 196

Bagnuolo, W. G., Jr., Furenlid, I. K., Gies, D. R., Barry, D. J., Russell, W. H., & Dorsey, J. F. 1990, PASP, 102, 604

Balona, L. A. 1995, MNRAS, 277, 1547

Bolton, C. T. 1983, Hvar Obs. Bull., 7, 141

Burger, M., de Jager, C., van den Oord, G. H. J., & Sato, N. 1982, A&A, 107, 320

Chiueh, T. 1997, ApJ, 482, L179

Cohen, D. H., Cassinelli, J. P., & MacFarlane, J. J. 1997, ApJ, 487, 867

Cranmer, S. R., Massa, D., & Owocki, S. P. 1996, AAS, 188, 5907

ESA (European Space Agency) 1997, The Hipparcos and Tycho Catalogues, ESA SP-1200 (ESA/ESTEC, Noordwijk)

Fullerton, A. W. 1999, in IAU Colloq. 169, Variable and Non-spherical Stellar Winds in Luminous Hot Stars, ed. B. Wolf, A. W. Fullerton, & O. Stahl (Heidelberg: Springer), in press

Fullerton, A., & Aerts, C. 1993, private comm. [FA93]

Fullerton, A., & Kaper, L. 1995, Hot Star Newsletter, 15, 2

Gies, D. R., Barry, D. J., Bagnuolo, W. G., Jr., Sowers, J., & Thaller, M. L. 1996, ApJ, 469, 884

Gies, D. R., & Kullavanijaya, A. 1988, ApJ, 326, 813 [GK88]

Gies, D. R., & Lambert, D. L. 1992, ApJ, 387, 673

Gies, D. R., & Wiggs, M. S. 1991, ApJ, 375, 321

Harmanec, P. 1987, IBVS, No. 3097

Harmanec, P. 1989, Bull. Astron. Inst. Czechosl., 40, 201

Harmanec, P. 1999, A&A, 341, 867 [H99]

Harmanec, P., & Tarasov, A. E. 1990, Bull. Astron. Inst. Czechosl., 41, 273

Howarth, I. D., Townsend, R. H. D., Clayton, M. J., Fullerton, A. W., Gies, D. R., Massa, D., Prinja, R. K., & Reid, A. H. N. 1998, MNRAS, 296, 949

Kambe, E., Ando, H., & Hirata, R. 1990, PASJ, 42, 687

Kambe, E., et al. 1997, ApJ, 481, 406

Kaper, L., et al. 1997, A&A, 327, 281

Kennelly, E. J., et al. 1998, ApJ, 495, 440

Kovacs, G. 1981, Ap&SS, 78, 175

Kurucz, R. L. 1994, Kurucz CD-ROM No. 19, Solar Abundance Model Atmospheres for 0,1,2,4,8 km/s (Cambridge: Smithsonian Astrophysical Observatory)

Mason, B. D., Gies, D. R., Hartkopf, W. I., Bagnuolo, W. G., Jr., ten Brummelaar, T., & McAlister, H. A. 1998, AJ, 115, 821

Massa, D., et al. 1995, ApJ, 452, L53

Penny, L. R. 1996, ApJ, 463, 737

Penny, L. R., Gies, D. R., & Bagnuolo, W. G., Jr. 1997, ApJ, 483, 439

Prinja, R. K. 1998, in Cyclical Variability in Stellar Winds, Proceedings of the ESO Workshop Held at Garching, Germany, 14 - 17 October 1997, ed. L. Kaper & A. W. Fullerton (Berlin: Springer), 92

Reid, A. H. N., & Howarth, I. D. 1996, A&A, 311, 616

Rivinius, Th., Baade, D., Stefl, S., Stahl, O., Wolf, B., & Kaufer, A. 1998a, A&A, 333, 125

Rivinius, Th., Baade, D., Stefl, S., Stahl, O., Wolf, B., & Kaufer, A. 1998b, A&A, 336, 177

Roberts, D. H., Lehár, J., & Dreher, J. W. 1987, AJ, 93, 968

Schneider, D. P., & Young, P. 1980, ApJ, 238, 946

Smith, M. A. 1985, ApJ, 288, 266

Smith, M. A. 1986, ApJ, 307, 213

Smith, M. A., Fullerton, A. W., & Percy, J. R. 1987, ApJ, 320, 768 [SFP87]

Tarasov, A. E., et al. 1995, A&AS, 110, 59 [T95]

Telting, J. H., & Schrijvers, C. 1997, A&A, 317, 723 [TS97]

Walborn, N. R. 1971, ApJS, 23, 357

Walborn, N. R., Parker, J. W., & Nichols, J. S. 1995, International Ultraviolet Explorer Atlas of B-type Spectra from 1200 to 1900 Å (NASA RP-1363) (Washington, DC: NASA)

This manuscript was prepared with the AAS LaTeX macros v4.0.

Fig. 1.— Radial velocities derived from the line wings of the UV ccfs (*open circles*) and Hα and He I λ6678 (average) (*filled circles*). The dotted line shows the prediction from T95 while the solid line shows the same curve translated in time to match better the observations.

Fig. 2.— A gray-scale depiction of the time evolution of the UV ccfs as a function of rest frame radial velocity. The lower panel shows the average ccf normalized to zero at the core and to one in the continuum. The upper frame shows differences from the mean as a gray-scale intensity. The white regions show gaps in the *IUE* coverage; the two short gray-scale segments bounded left and right by white regions represent MTT spectra of He I λ6678 observed during two of the gaps.

Fig. 3.— A gray-scale depiction of the time evolution of the MTT optical spectra as a function of rest frame radial velocity. The lower frame shows the global average spectrum while the upper gray-scale image illustrates the differences from the mean as a function of time and wavelength. Arrows at right indicate the times of mid-exposure.

Fig. 4.— A comparison of normalized difference profiles for the UV ccfs (*solid lines*) and the smoothed He I λ6678 line (*dotted lines*) during an interval of simultaneous coverage. The difference profiles are arranged so that their continuum levels are aligned with the time of observation. The amplitude relative to core line depth is indicated by the bar in the upper right.

Fig. 5.— The window functions for the data sampling of the *IUE* (*above*) and MTT (*below*) spectra of ϵ Per. The window functions show the pattern of alias signals (introduced by sampling) that will surround any actual periodic signal (set at a frequency of 6 d^{-1} in this case).

Fig. 6.— A gray-scale representation of the UV ccf power spectra as a function of position in the profile and frequency. Periodicities appear as dark, horizontal bars. The mean UV ccf is plotted below.

Fig. 7.— A sequence of observed and modeled summed periodograms of line intensity variations in ϵ Per. The top panel is the summed periodogram for MTT observations of He I λ6678 while the third panel down is the same for the UV ccfs (from contemporary *IUE* observations.) The second panel illustrates the expected appearance of the periodogram for the MTT, optical time series based on a convolution of the UV-detected signals (shown as vertical dashed lines in the middle panel) with the MTT window function (Fig. 5). The fifth panel down shows the summed periodogram for Si III λ4552 variations observed in 1986 together with the signals found by GK88 (vertical dashed lines). The fourth panel down plots the expected periodogram for the 1986 sequence based on the signal frequencies and amplitudes from the 1996 *IUE* data convolved with the 1986 window function. The sixth (bottom) panel shows the periodogram for the short time series of *IUE* spectra from 1984 (Fig. 8).

Fig. 8.— A gray-scale depiction of the time evolution of the UV ccfs from 13 spectra made on 1984 November 2 (same format as Fig. 2).

Fig. 9.— A series of amplitude and phase diagrams for the 6 main periodic signals found in the UV ccfs. The top panel for each signal shows the distribution of semi-amplitude across the profile (normalized to the ccf maximum) while the lower panel gives the variation in complex phase (in units of π radians).

Fig. 10.— The power distribution of the UV ccfs after Fourier transformation in the wavelength dimension (Kennelly et al. 1998). The power is illustrated here as a function of "apparent" NRP degree, l, and frequency.

Fig. 11.— The time variations in the equivalent widths of the strong, wind-related lines of C IV λ1550 and Si IV λ1400. The normalized deviations (relative to a mean of 1) of the C IV (*asterisks*) and Si IV (*diamonds*) equivalent widths are offset by +0.4 and +0.3, respectively, for clarity. The normalized excursions of the UV ccfs at the line center position are plotted below (*plus signs*) together with the 6-sinusoid model (*solid line*) at an offset position of +0.15.

Table 1. IUE Radial Velocity Measurements

SWP Image	HJD (2,450,000+)	V_r (km s^{-1})
56399	92.9275	−1.5
56400	92.9496	1.1
56401	92.9768	0.1
56402	92.9984	−2.4
56403	93.0187	2.1
56404	93.0410	−2.6
56405	93.0619	−5.5
56406	93.0819	0.3
56407	93.1029	−0.7
56408	93.1237	−2.8
56409	93.1446	−3.6
56410	93.1641	7.6
56411	93.1873	6.4
56412	93.2063	11.6
56413	93.2376	1.1
56414	93.2614	2.8
56415	93.2834	−3.0
56416	93.3052	−0.9
56417	93.3295	−0.8
56418	93.3502	5.2
56419	93.3718	7.0
56420	93.3949	11.6
56421	93.4195	3.7
56422	93.4437	1.3

Table 1—Continued

SWP Image	HJD (2,450,000+)	V_r (km s^{-1})
56423	93.4753	3.9
56424	93.5051	5.5
56425	93.5256	9.1
56426	93.5479	13.1
56427	93.6979	10.7
56428	93.7194	5.9
56429	93.7384	9.2
56430	93.7584	8.9
56431	93.7840	0.6
56432	93.8102	2.7
56433	93.8418	2.5
56434	93.8651	5.7
56435	93.8869	5.4
56436	93.9093	11.8
56437	93.9394	7.9
56438	93.9616	7.6
56439	93.9848	3.7
56440	94.0119	0.8
56441	94.0364	3.5
56442	94.0701	2.2
56443	94.0925	6.5
56444	94.1142	5.3
56445	94.1417	7.3
56446	94.1629	8.6

Table 1—Continued

SWP Image	HJD (2,450,000+)	V_r (km s^{-1})
56447	94.1828	4.8
56448	94.2112	12.0
56449	94.2381	11.4
56450	94.2618	3.9
56451	94.2864	7.5
56452	94.3161	11.4
56453	94.3434	11.1
56454	94.3669	15.4
56455	94.4042	2.2
56456	94.4295	1.7
56457	94.4538	0.5
56458	94.5319	15.9
56459	94.5585	12.7
56460	94.6931	7.6
56461	94.7165	13.1
56462	94.7372	14.7
56463	94.7592	6.7
56464	94.7782	3.9
56465	94.8045	1.4
56466	94.8311	3.5
56467	94.8664	7.1
56468	94.8890	10.1
56469	94.9092	13.8
56470	94.9308	9.1

Table 1—Continued

SWP Image	HJD (2,450,000+)	V_r (km s^{-1})
56471	94.9508	6.8
56472	94.9822	6.2
56473	95.0119	8.0
56474	95.0350	10.1
56475	95.0685	16.2
56476	95.0908	12.5
56477	95.1108	12.8
56478	95.1375	8.8
56479	95.1589	7.8
56480	95.1800	8.1
56481	95.2507	11.1
56482	95.2704	9.6
56483	95.3019	14.5
56484	95.3272	8.0
56485	95.3476	3.4
56486	95.3757	10.2
56487	95.4017	8.0
56488	95.4282	8.1
56489	95.4551	11.6
56490	95.4897	10.9
56491	95.5109	5.1
56492	95.5310	5.6
56493	95.5547	7.3
56494	95.6903	7.7

Table 1—Continued

SWP Image	HJD (2,450,000+)	V_r (km s^{-1})
56495	95.7155	9.1
56496	95.7368	8.4
56497	95.7564	13.9
56498	95.7790	12.5
56499	95.8001	11.4
56500	95.8260	11.0
56501	95.8473	12.0
56502	95.8697	10.7
56503	95.8969	13.3
56504	95.9175	11.5
56505	95.9452	12.4
56506	95.9670	8.1
56507	95.9881	6.3
56508	96.0182	11.4
56509	96.0386	9.6
56510	96.0589	9.2
56511	96.0830	16.7
56512	96.1039	8.8
56513	96.1286	5.0
56514	96.1486	2.8
56515	96.1710	2.6
56516	96.1972	8.8
56517	96.2241	16.1
56518	96.2507	13.9

Table 1—Continued

SWP Image	HJD (2,450,000+)	V_r (km s^{-1})
56519	96.2736	6.4
56520	96.2970	9.2
56521	96.3191	8.7
56522	96.3418	2.0
56523	96.3633	9.3
56524	96.3917	11.6
56525	96.4184	13.2
56526	96.4459	11.6
56527	96.4663	12.2
56528	96.4864	4.6
56529	96.5077	3.2
56530	96.5302	6.0
56531	96.6822	10.6
56532	96.7021	14.6
56533	96.7213	15.6
56534	96.7410	19.2
56535	96.7612	17.4
56536	96.7821	18.5
56537	96.8016	16.1
56538	96.8218	12.1
56539	96.8439	12.6
56540	96.8648	8.6
56541	96.8844	14.8
56542	96.9055	14.6

Table 1—Continued

SWP Image	HJD (2,450,000+)	V_r (km s^{-1})
56543	96.9292	10.6
56544	96.9491	16.9
56545	96.9688	12.0
56546	96.9906	14.2
56547	97.0122	8.8
56548	97.0323	12.2
56549	97.0539	16.6
56550	97.0748	18.2
56551	97.0958	16.2
56552	97.1253	11.4
56553	97.1472	18.7
56554	97.1713	17.4
56555	97.2035	22.6
56556	97.2242	14.4
56557	97.2534	13.7
56558	97.2740	15.0
56559	97.3007	14.0
56560	97.3375	7.7
56561	97.3578	8.6
56562	97.3836	12.8
56563	97.4093	13.3
56564	97.4393	12.1
56565	97.4619	13.1
56566	97.4830	13.8

Table 1—Continued

SWP Image	HJD (2,450,000+)	V_r (km s^{-1})
56567	97.5036	11.5
56568	97.5235	9.9
56569	97.5501	19.3
56570	97.6822	15.1
56571	97.7124	19.4
56572	97.7341	20.8
56573	97.7531	14.8
56574	97.7731	13.6
56575	97.8007	10.9
56576	97.8236	13.3
56577	97.8455	16.3
56578	97.8706	19.8
56579	97.8927	18.8

Table 2. MTT Radial Velocity Measurements

HJD (2,450,000+)	V_r(Hα) (km s^{-1})	V_r(He I λ6678) (km s^{-1})	$< V_r >$ (km s^{-1})
91.589	−4.9	−2.5	−3.7
91.629	1.0	3.1	2.1
91.652	3.3	−0.3	1.5
91.668	−6.0	−4.8	−5.4
91.719	−1.2	−1.9	−1.6
91.747	−4.9	−8.1	−6.5
91.768	−0.5	−0.7	−0.6
91.783	4.1	0.8	2.4
91.806	2.8	−0.2	1.3
91.821	18.0	16.2	17.1
92.728	5.2	2.0	3.6
92.744	10.0	4.2	7.1
92.766	1.6	1.2	1.4
92.803	5.2	3.3	4.3
93.563	6.8	10.5	8.6
93.578	7.2	5.9	6.6
93.593	6.6	2.4	4.5
93.619	7.5	7.6	7.6
93.633	6.2	1.6	3.9
93.651	1.2	−3.5	−1.1
93.665	9.7	4.9	7.3
96.543	5.6	8.4	7.0
96.560	7.1	9.1	8.1
96.576	−1.0	0.3	−0.4

Table 2—Continued

HJD (2,450,000+)	V_r(Hα) (km s^{-1})	V_r(He I λ6678) (km s^{-1})	$< V_r >$ (km s^{-1})
96.593	14.3	18.5	16.4
96.614	16.9	14.8	15.9
96.637	19.2	14.4	16.8
96.668	15.9	11.7	13.8
96.704	16.6	15.0	15.8
96.718	14.7	15.0	14.9
96.734	18.1	18.2	18.1
96.749	26.7	26.5	26.6
96.765	20.7	24.6	22.6
96.781	24.5	28.5	26.5
96.804	15.5	12.9	14.2
96.820	17.9	17.6	17.7
103.646	0.2	4.7	2.4
103.662	−11.5	−8.8	−10.2
103.686	−8.1	−8.2	−8.2
103.712	−9.3	−9.0	−9.2
103.737	−7.0	−4.7	−5.8
103.759	−10.4	−11.0	−10.7
103.777	−8.6	−8.7	−8.7
103.793	−2.3	−9.3	−5.8
104.551	0.6	4.9	2.7
104.617	−3.7	−7.8	−5.8
104.637	−7.7	−12.2	−9.9
104.651	−6.1	−10.6	−8.4

Table 2—Continued

HJD (2,450,000+)	V_r(Hα) (km s^{-1})	V_r(He I λ6678) (km s^{-1})	$< V_r >$ (km s^{-1})
104.666	-2.1	0.4	-0.8
104.685	-1.8	-5.8	-3.8
104.701	-2.5	-1.2	-1.9
104.715	1.2	0.4	0.8
104.735	-5.4	-2.0	-3.7
104.751	-5.2	-5.5	-5.4

Table 3. Periods From Time Series Analysis

No.	AIC(MSF)	P(MSF) (hr)	P(PW) (hr)	P(DP) (hr)	P(Hα) (hr)	P(He I λ6678) (hr)
0	74227	···	···	···	···	···
1	58323	4.0638(4)	4.0477(4)	4.05(7)	4.078(26)	4.076(26)
2	50530	4.5436(5)	4.5384(5)	4.54(9)	4.555(33)	4.554(33)
3	42466	3.8370(4)	3.8473(4)	3.86(6)	3.830(23)	3.829(23)
4	37729	2.26836(13)	2.26837(13)	2.269(22)	···	2.271(8)
5	34513	8.4634(18)	8.4754(18)	8.43(30)	···	···
6	31453	24.469(15)	24.603(15)	23.8(24)	···	···
7	29309	3.5089(3)	3.5100(3)	3.51(5)	···	···

Table 4. Comparison With Periods From Prior Work

1996 (IUE + MTT)		1984 (KPNO)	1986 (McDonald)				1989 (Crimea)
Frequency (d^{-1})	P(MSF) (hr)	P(SFP87) (hr)	P(GK88) (hr)	P(FA93) (hr)	P(TS97) (hr)	P(MSF) (hr)	P(H99) (hr)
2.8357(6)	8.4634(18)	···	···	···	···	···	···
5.2822(6)	4.5436(5)	···	4.466(23)	4.457	4.47(7)	4.5041(7)	···
5.9058(6)	4.0638(4)	···	···	···	···	4.0497(6)	···
6.2549(7)	3.8370(4)	3.85(2)	3.837(5)	3.822	3.83(6)	3.8232(5)	3.835822(8)
6.8398(6)	3.5089(3)	···	···	3.480	3.46(4)	3.4869(4)	···
7.905[a]	···	···	3.036(10)	···	···	···	···
10.5803(6)[b]	2.26836(13)	2.25(3)	2.264(12)	2.265	2.26(2)	2.2648(2)	···
12.53[c]	···	···	···	···	1.92(1)	···	···

[a]Mistaken alias of the 6.84 d^{-1} signal.

[b]Possible first harmonic of the 5.28 d^{-1} signal.

[c]Possible first harmonic of the 6.25 d^{-1} signal.

Table 5. Estimates of NRP Degree l from Phase Differences Across the Profile

Freq. (d^{-1})	P (hr)	IUE	IUE[a]	IUE[b]	He I λ6678	Hα	Si III λ4552	GK88	TS97	Adopted
2.8357	8.4634	2.8	3.0	3.7	⋯	⋯	⋯	⋯	⋯	3 ± 1
5.2822	4.5436	2.9	3.1	4.1	2.8	2.9	2.8	3	3.1	3 ± 1
5.9058	4.0638	2.7	3.3	4.8	2.9	2.5	3.0	⋯	⋯	3 ± 1
6.2549	3.8370	3.3	3.6	4.4	3.1	3.0	3.5	4	4.2	4 ± 1
6.8398	3.5089	3.4	4.2	5.5	⋯	⋯	4.2	⋯	5.0	4 ± 1
10.5803	2.2684	3.4	5.6	6.6	4.2	⋯	4.9	6	5.5[c]	5 ± 1

[a]Kennelly et al. (1998) method.

[b]$d\Psi/dV_r$ method.

[c]$l = 3.1, |m| = 2.0$ if this signal is the harmonic of the 4.54 hr signal.

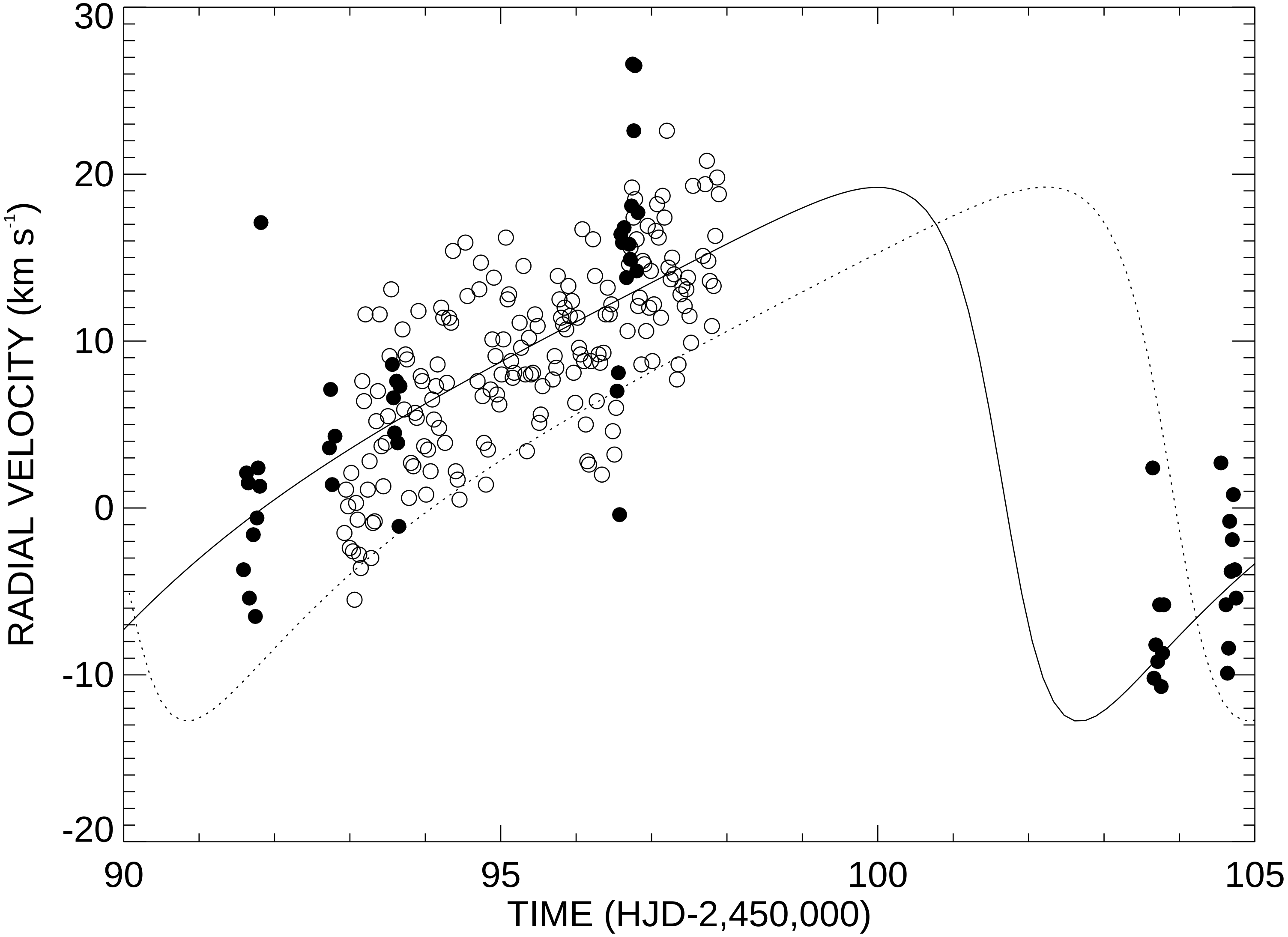
RADIAL VELOCITY (km s^{-1})
30
20
10
0
-10
-20
90
95
100
105
TIME (HJD-2,450,000)

Fig. 1.—

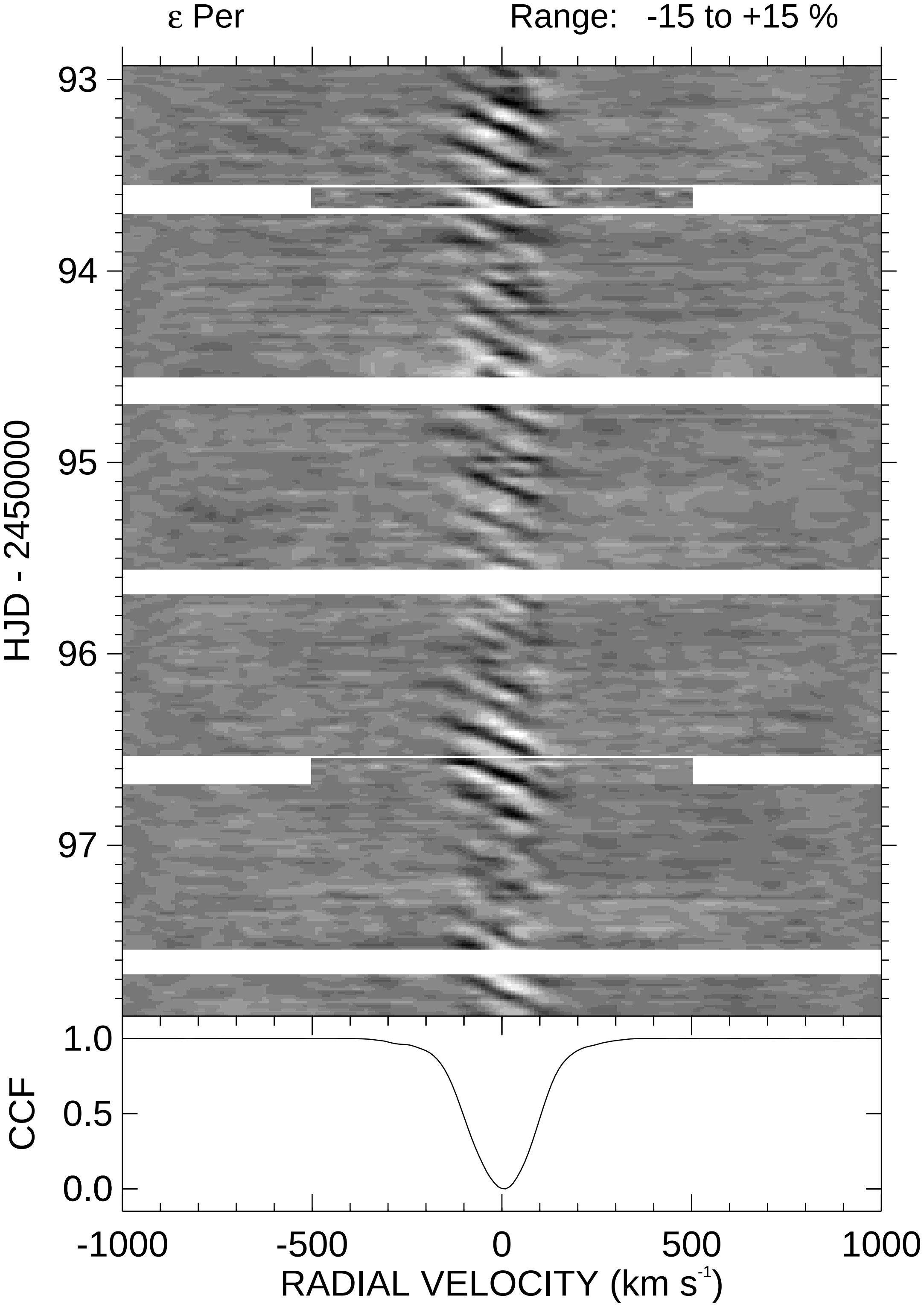
ε Per
Range: -15 to +15 %
HJD - 2450000
93
94
95
96
97
CCF
1.0
0.5
0.0
-1000
-500
0
500
1000
RADIAL VELOCITY (km s-1)

Fig. 2.—

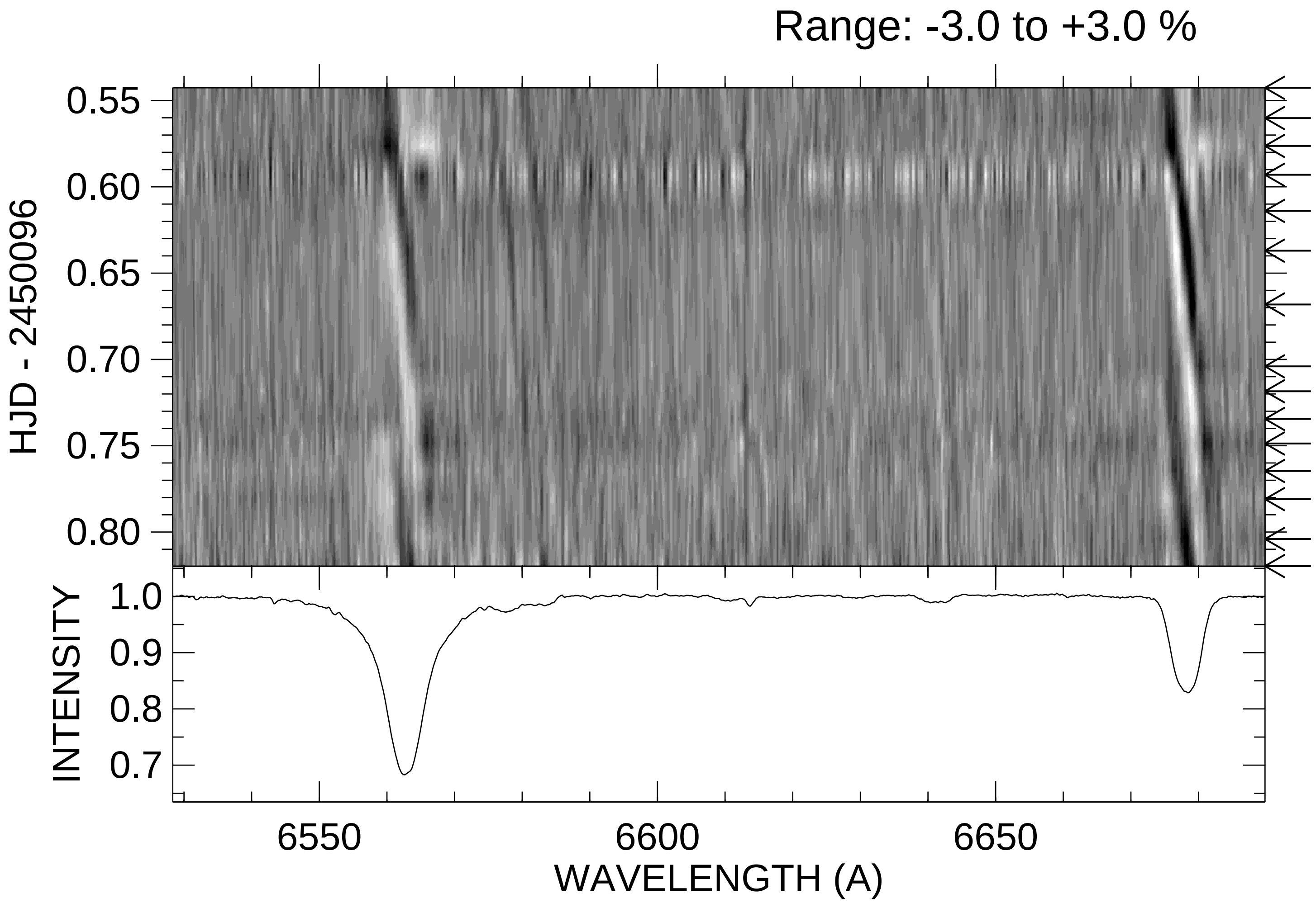

Range: -3.0 to +3.0 %
HJD - 2450096
0.55
0.60
0.65
0.70
0.75
0.80
INTENSITY
1.0
0.9
0.8
0.7
6550
6600
6650
WAVELENGTH (A)

Fig. 3.—

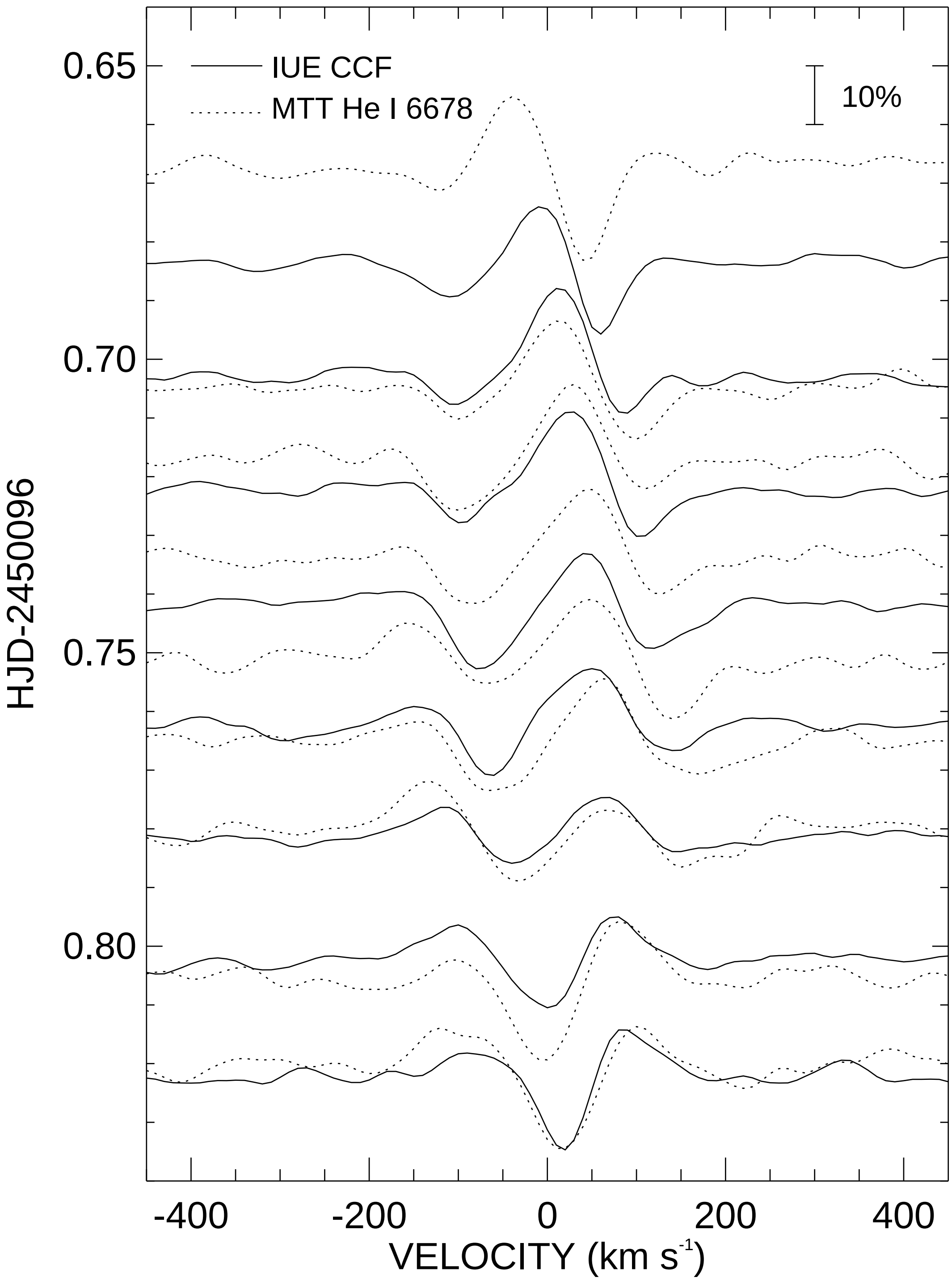

IUE CCF
MTT He I 6678
10%
0.65
0.70
0.75
0.80
HJD-2450096
-400
-200
0
200
400
VELOCITY (km s-1)

Fig. 4.—

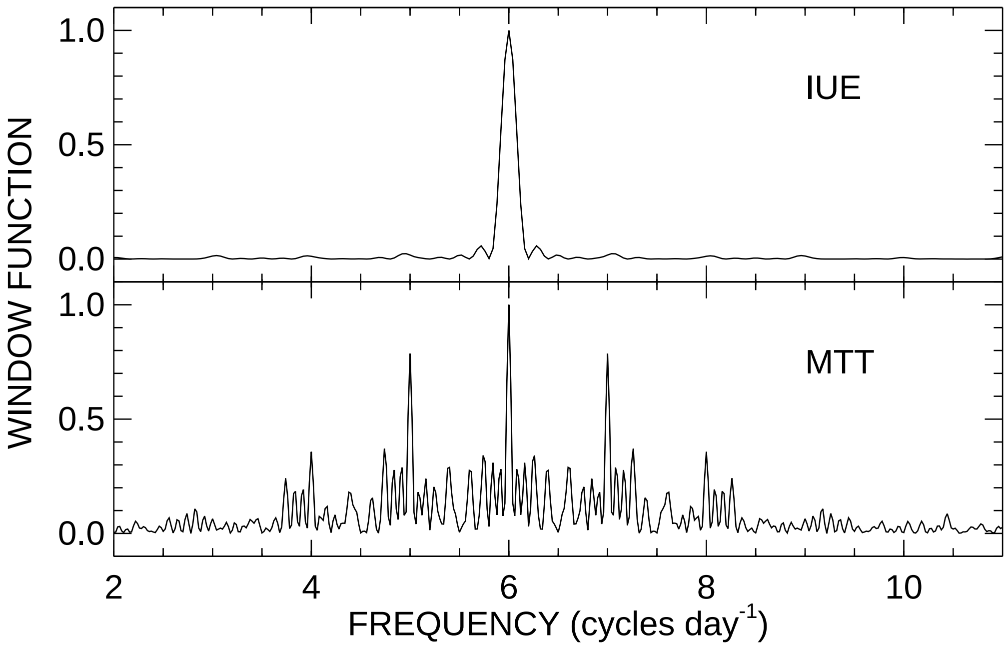
WINDOW FUNCTION
1.0
0.5
0.0
IUE
MTT
2
4
6
8
10
FREQUENCY (cycles day-1)

Fig. 5.—

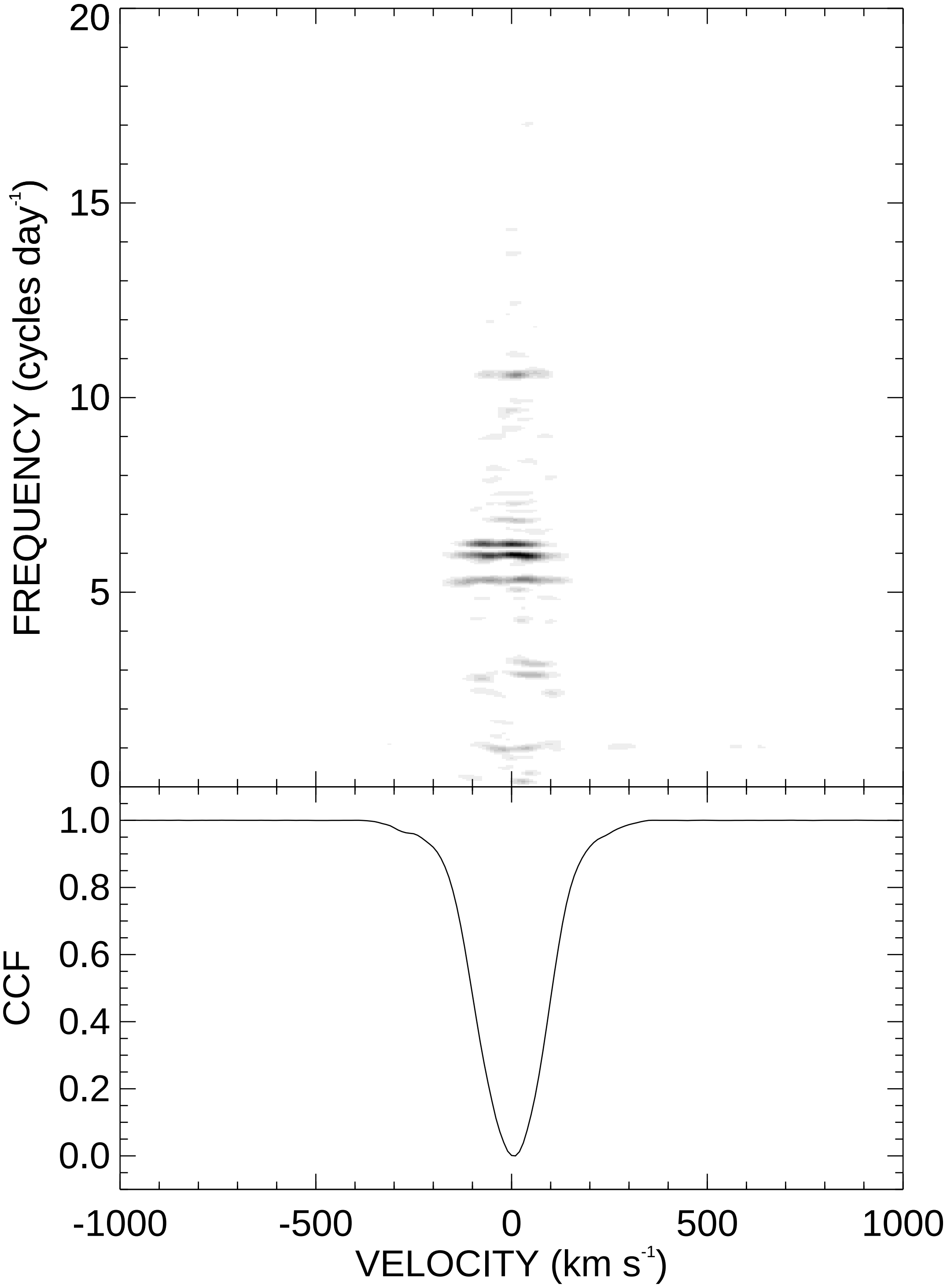
20
15
10
5
0
FREQUENCY (cycles day^{-1})
1.0
0.8
0.6
0.4
0.2
0.0
CCF
-1000
-500
0
500
1000
VELOCITY (km s^{-1})

Fig. 6.—

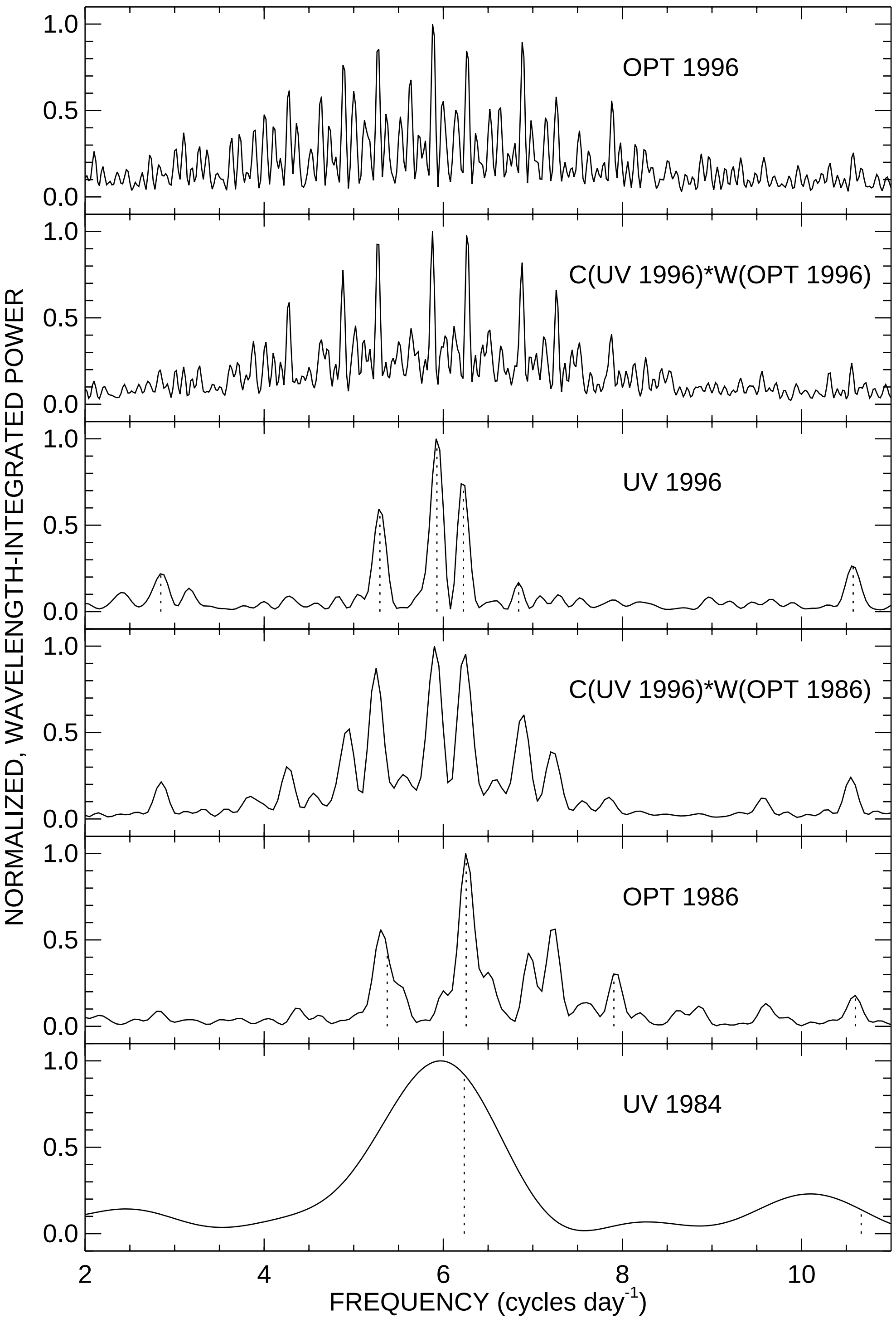

OPT 1996
C(UV 1996)*W(OPT 1996)
UV 1996
C(UV 1996)*W(OPT 1986)
OPT 1986
UV 1984
NORMALIZED, WAVELENGTH-INTEGRATED POWER
FREQUENCY (cycles day-1)

Fig. 7.—

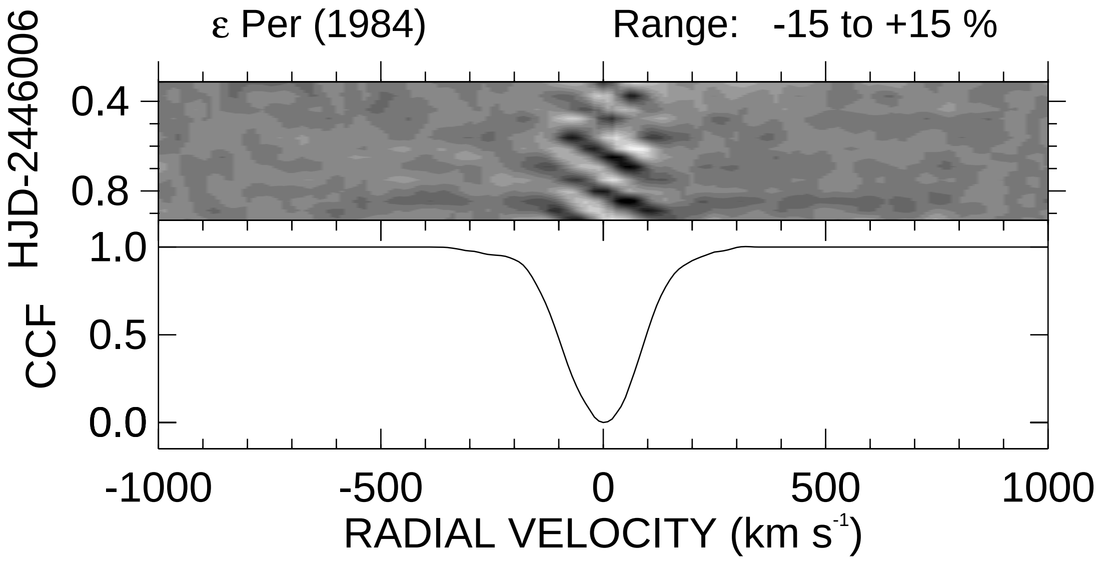
ε Per (1984)
Range: -15 to +15 %
HJD-2446006
0.4
0.8
1.0
CCF
0.5
0.0
-1000
-500
0
500
1000
RADIAL VELOCITY (km s-1)

Fig. 8.—

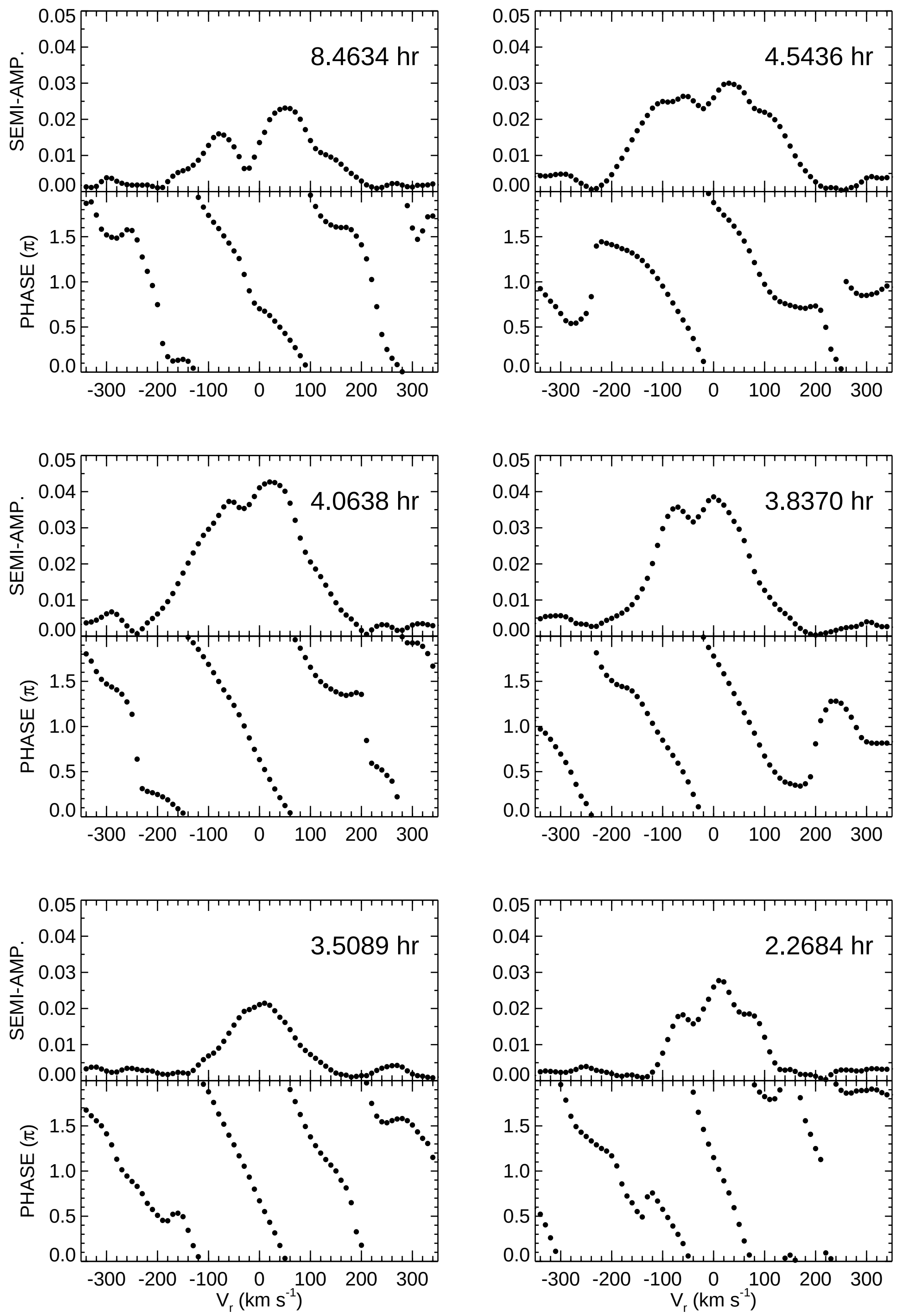
8.4634 hr
4.5436 hr
4.0638 hr
3.8370 hr
3.5089 hr
2.2684 hr
SEMI-AMP.
PHASE (π)
V_r (km s^-1)

Fig. 9.—

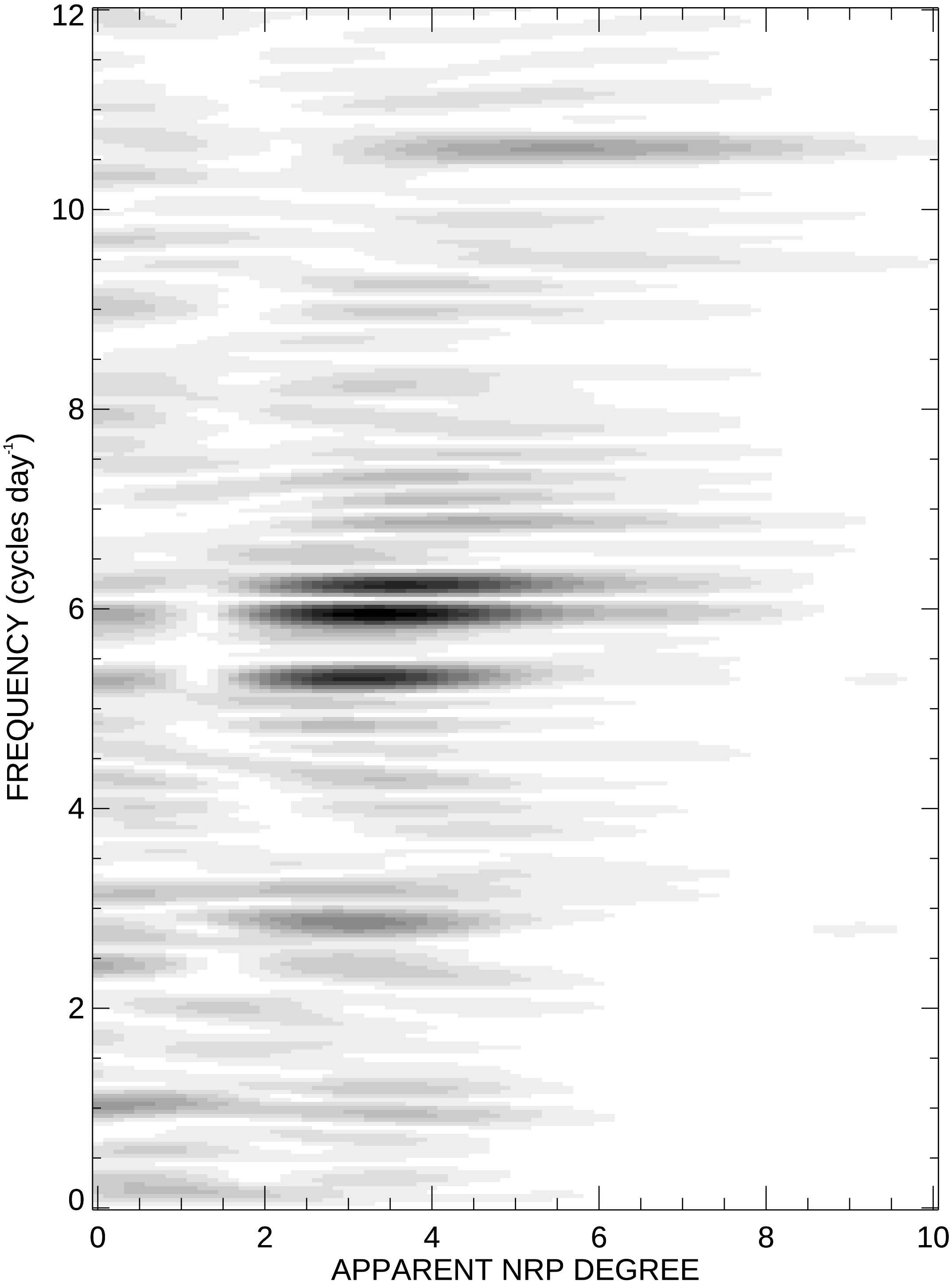

Fig. 10.—

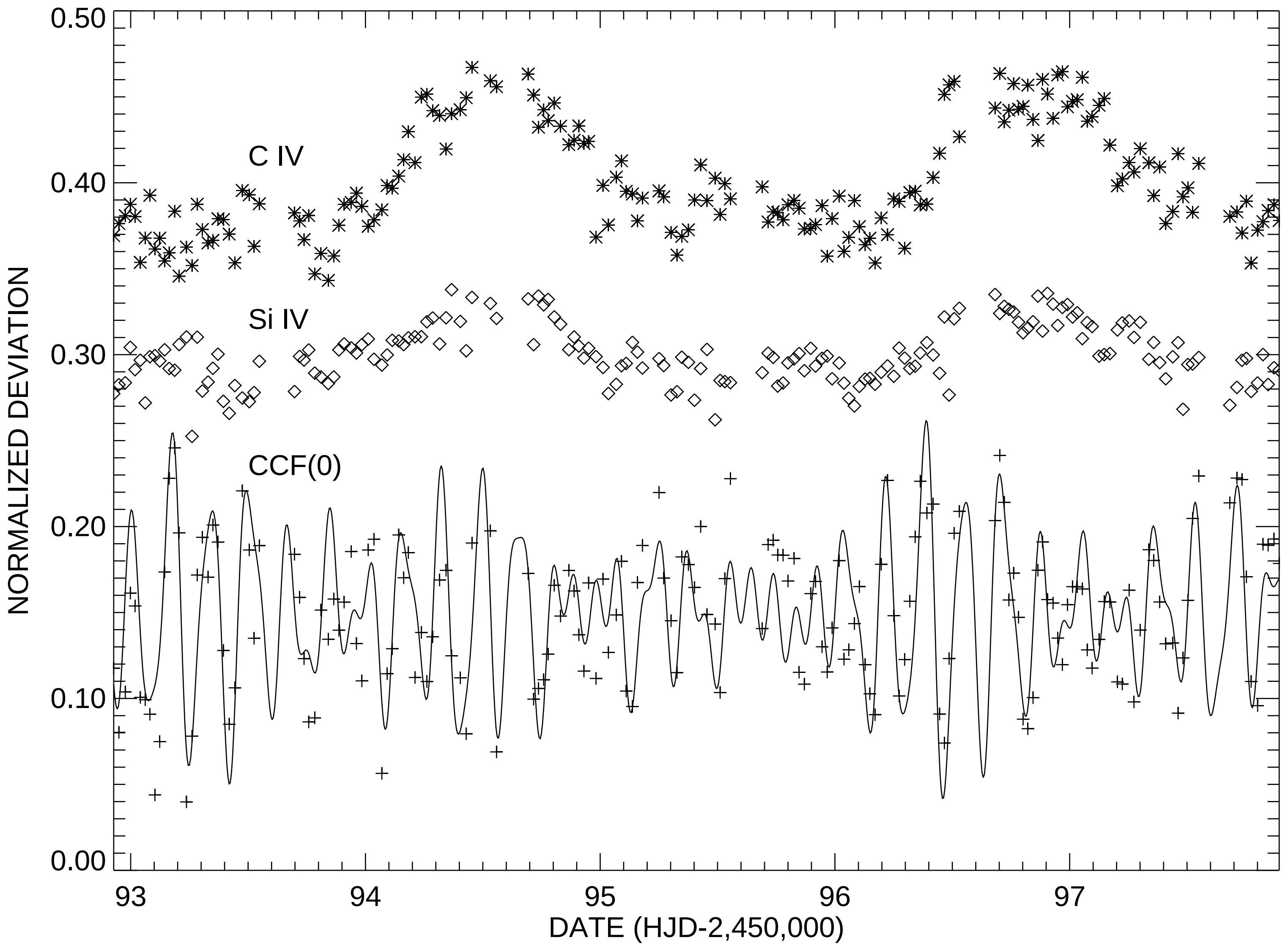
NORMALIZED DEVIATION
0.00
0.10
0.20
0.30
0.40
0.50
C IV
Si IV
CCF(0)
93
94
95
96
97
DATE (HJD-2,450,000)

Fig. 11.—